Monthly Notices of the ROYAL ASTRONOMICAL SOCIETY

MNRAS **512,** 1967–1984 (2022) https://doi.org/10.1093/mnras/stac431
Advance Access publication 2022 February 17

Model-independent constraints on $\Omega_{\rm m}$ and $H(z)$ from the link between geometry and growth

Jaime Ruiz-Zapatero [1]★ Carlos García-García,[1] David Alonso,[1] Pedro G. Ferreira[1] and Richard D. P. Grumitt[2]

[1]*Department of Physics, University of Oxford, Denys Wilkinson Building, Keble Road, Oxford OX1 3RH, United Kingdom*
[2]*Department of Astronomy, Tsinghua University, Beijing 100084, China*

Accepted 2022 February 14. Received 2022 February 14; in original form 2022 January 18

ABSTRACT

We constrain the expansion history of the Universe and the cosmological matter density fraction in a model-independent way by exclusively making use of the relationship between background and perturbations under a minimal set of assumptions. We do so by employing a Gaussian process to model the expansion history of the Universe from present time to the recombination era. The expansion history and the cosmological matter density are then constrained using recent measurements from cosmic chronometers, Type-Ia supernovae, baryon acoustic oscillations, and redshift-space distortion data. Our results show that the evolution in the reconstructed expansion history is compatible with the *Planck* 2018 prediction at all redshifts. The current data considered in this study can constrain a Gaussian process on $H(z)$ to an average 9.4 per cent precision across redshift. We find $\Omega_{\rm m} = 0.224 \pm 0.066$, lower but statistically compatible with the *Planck* 2018 cosmology. Finally, the combination of future DESI measurements with the CMB measurement considered in this work holds the promise of 8 per cent average constraints on a model-independent expansion history as well as a five-fold tighter $\Omega_{\rm m}$ constraint using the methodology developed in this work.

Key words: gravitational lensing: weak – methods: data analysis – cosmological parameters – large-scale structure of Universe – cosmology: theory.

1 INTRODUCTION

When observing and characterizing the Universe on large scales, there are two broadly different, yet intertwined, types of observations (Peebles 1980). In the first type of observation, one endeavours to constrain the expansion rate of the Universe at different times. This can be done by measuring the expansion rate itself or through a variety of cosmological distance measures: angular diameter distances, luminosity distances, standard sirens, etc. In particular, if $a(t)$ is the scale factor of the Universe at cosmic time t, the expansion rate at that time can be defined as $H[a(t)] = \dot{a}/a$ (where the overdot is derivative with regard to cosmic time). Then, one can derive an expression for the radial comoving distance, $D_{\rm M}$, by following a radial null-geodesic.

$$D_{\rm M} \equiv \chi = \int_t^{t_0} \frac{dt'}{a(t')} = \int_0^z \frac{dz'}{H(z')}, \tag{1}$$

where we use unit $c = 1$ throughout, t_0 is cosmic time today, and z is the cosmological redshift, $1 + z = 1/a$. Moreover, assuming zero spatial curvature, it is possible to derive expressions for the luminosity ($D_{\rm L}$) and angular diameter distances ($D_{\rm A}$) by multiplying and dividing equation (1) by $(1 + z)$, respectively:

$$D_{\rm L} = (1+z)D_{\rm M} \quad \text{and} \quad D_{\rm A} = D_{\rm M}/(1+z). \tag{2}$$

Thus, measurements of $D_{\rm L}$ and $D_{\rm A}$ at different redshifts can be used to reconstruct $H(z)$ over time.

In the second type of observation, one focuses on the rate with which structures undergo gravitational collapse on the expanding background. Under the assumptions that the bulk of matter in the recent past can be described by a presureless fluid and that neutrino effects can be neglected, the density contrast, $\delta \equiv \rho/\bar{\rho} - 1$ (where $\bar{\rho}$ is the mean matter density of the Universe), obeys an evolution equation of the form:

$$f' + f^2 + \left(1 + \frac{{\rm d}\ln aH}{{\rm d}\ln a}\right) f = \frac{3}{2}\Omega_{\rm m}(z), \tag{3}$$

where the prime denotes a derivative with regard to $\ln a$, the growth rate is defined as $f \equiv {\rm d}\ln\delta/{\rm d}\ln a$, and $\Omega_{\rm m}(z)$ is the fractional energy density in matter as a function of redshift. The latter quantity depends, through the Einstein field equations, on $H \equiv H(z)$ so that

$$\Omega_{\rm m}(z) = \frac{\Omega_{\rm m} H_0^2}{a^3 H^2}, \tag{4}$$

with $\Omega_{\rm m} \equiv \Omega_{\rm m}(0)$, which we use for ease of notation. Thus, a measurements of the growth rate of structure at different redshifts (or times) can also be used to reconstruct $H(z)$ over time as well as the fractional matter density today, $\Omega_{\rm m}$.

The challenge of modern cosmology has been to use a wide range of different cosmological observables to constrain $H(z)$ as a function of time or redshift (and, of course, $\Omega_{\rm m}$) and, crucially, to pin down the underlying cosmological model, which describes $H(z)$ in terms of

★ E-mail: jaime.ruiz-zapatero@physics.ox.ac.uk

a greatly reduced set of cosmological parameters. The frontrunner is the Λ Cold Dark Matter (ΛCDM) model, whose parameters are now constrained to an unprecedented precision (Planck Collaboration VI 2020). However, interestingly, inconsistencies, or 'tensions', have begun to emerge. Different probes are leading to different constraints on, for example, the Hubble constant, H_0 (e.g. Freedman et al. 2020; Pesce et al. 2020; Riess et al. 2021) or the density-weighted amplitude of fluctuations, $S_8 \equiv \sigma_8(\Omega_m/0.3)^{0.5}$ (e.g. Alsing, Heavens & Jaffe 2017; Asgari et al. 2021; DES Collaboration 2021; García-García et al. 2021; Heymans et al. 2021; Nunes & Vagnozzi 2021; Ruiz-Zapatero et al. 2021; White et al. 2021), where σ_8 is the variance of δ, in spheres of radius $8\,h^{-1}$Mpc.

In this paper, we ask if it is possible to obtain meaningful, or precise, constraints on cosmological parameters with minimal assumptions about the cosmological model. To be more specific, we step back and try to find model-independent constraints on $H(z)$ and Ω_m from measurements of the expansion history itself, cosmological distances, and the growth rate. This allows us to contrast the constraining power of these two very different sets of observables to explore how combining them improves constraints and, most importantly, how much constraints improve once one assumes a cosmological model. The hope is that understanding this process will shed light on the analysis of theories that go beyond ΛCDM but may also have bearing on the current inconsistencies in parameter constraints. We will implement our model-independent approach using Gaussian processes (GPs) (Rasmussen & Williams 2006; Seikel, Clarkson & Smith 2012). Gaussian processes allow us to reconstruct a well-defined distribution of histories of $H(z)$. The data then allow us to constrain the parameters of this distribution and, in doing so, tell us at what redshifts $H(z)$ is well determined and at what redshifts it is determined poorly.

The literature already hosts a number of examples of the possible uses of GPs to test certain aspects of the present cosmological paradigm in model-agnostic ways. For example, one can find tests for the model dependence of the H_0 (Gómez-Valent & Amendola 2018; Cai, Khurshudyan & Saridakis 2020; Liao et al. 2020; Bonilla, Kumar & Nunes 2021) and S_8 (L'Huillier, Shafieloo & Kim 2018; Benisty 2021) tensions for the non-zero curvature of space–time (Shafieloo, L'Huillier & Starobinsky 2018; Vagnozzi, Loeb & Moresco 2021; Yang & Gong 2021), as well as tests for the density and the equation of state of dark energy (Zhang & Li 2018; Gerardi, Martinelli & Silvestri 2019). More closely related to the topic of this work, in Perenon et al. (2021), GPs were used to study the statistical correlations between the expansion history, cosmological distances, and the linear growth rate without appealing to the physical relationships between the three functions. However, the clearest precedent of the methodology used here is Li et al. (2021), who already employ GPs to obtain model-independent constraints for Ω_m and σ_8 based on the relationship between the expansion history and the linear growth rate. The methodology developed in the present paper expands and improves many aspects of their analysis. First, our GP extends all the way to recombination. This allows us to solve the Jeans equation (equation 3) without using fitting formulas. Moreover, we also employ cosmological distances to constrain the evolution of the expansion history. This, in combination with the extended range of the GP, allows us to use the position of the first acoustic peak of the CMB temperature power spectrum to constrain expansion history far into the past. Finally, and most importantly, we sample our GP simultaneously with the cosmological parameters, allowing us to observe potential correlations between the two.

The structure of this paper is as follows: in Section 2, we present the methodology of this work regarding the use of GP to compute predictions for cosmological observables. In Section 3, we describe the cosmological observables from which we employ data and motivate their use in the context of this work. We present our results in Section 4 and discuss the implications of our work in Section 5.

2 METHODOLOGY

Throughout this paper, we will be working with the equations (1) and (3) to connect the time evolution of $H(z)$ with current and future observations. In the case of direct measurements of $H(z)$, the expansion history can be trivially matched to observations without the need to apply any transformation. In the case of distances, we can see from equation (1) that it is possible to generate predictions for the observables from any choice of $H(z)$ by performing the relevant integral. In the case of growth (equation 3), we are faced with the problem that most observations do not report f but the combined quantity $f\sigma_8$. Thus, it is convenient to rewrite equation (3) in terms of the latter. This can be done as follows: assuming that perturbations grow in a self-similar manner, we can define $\delta(t, \mathbf{x}) \equiv D(t)\delta_0(\mathbf{x})$, where δ_0 is the density contrast today. Then, we can rewrite equation (3) as

$$\frac{d}{da}\left(a^2 H \frac{dD}{d\log a}\right) = \frac{3}{2}\Omega_m(a)\, a\, H\, D. \tag{5}$$

Defining $y \equiv a^2 E \frac{dD}{d\log a}$, with $E \equiv H/H_0$, and switching to the integration variable $s \equiv \log(1+z)$, this equation can be written in terms of a system of coupled first-order equations:

$$\frac{dy}{ds} = -\frac{3}{2}\frac{\Omega_m}{aE} D\,, \qquad \frac{dD}{ds} = -\frac{y}{a^2 E}. \tag{6}$$

Then, it is possible to transform the quantities $y(s)$ and $D(s)$ into $f\sigma_8(s)$ and $\sigma_8(s)$ by applying the following transformation

$$\sigma_8(s) = \sigma_8(0)\frac{D(s)}{D(0)}\,, \qquad f\sigma_8(s) = \frac{y(s)\,\sigma_8(0)}{E(s)D(0)} e^{2s}. \tag{7}$$

The thrust of this paper is to keep the analysis as model-independent as possible. Yet, as we can see, it is still possible to extract information about some of the cosmological parameters. For a start, combining the information from distances and growth allows us to constrain Ω_m. But we also have, automatically, $H_0 \equiv H(z=0)$ and, as we just saw, we can calculate $\sigma_8 \equiv \sigma_8(z=0)$ (or S_8 as a derived parameter).

In this paper, we will model the time (or redshift)-dependent Hubble rate, $H(z)$, as a GP spanning over the redshift range $0 < z < 1100$. A GP is a collection of random variables, any finite number of which have a joint Gaussian distribution (Rasmussen & Williams 2006). A GP $g(\mathbf{x})$, where $\boldsymbol{x}$ is a collection of random variables, is fully specified by a mean function $m(\mathbf{x}) \equiv \mathcal{E}[g(\mathbf{x})]$, where $\mathcal{E}[\cdots]$ is the expectation value over the ensemble, and a covariance function $k(\mathbf{x}, \mathbf{x}') \equiv \mathcal{E}[(g(\mathbf{x}) - m(\mathbf{x}))(g(\mathbf{x}') - m(\mathbf{x}'))^T]$. In combination, the mean and covariance functions determine the statistical properties of the ensemble of random variables, which defines the family of shapes that the GP can take.

Thus, GPs can be used as agnostic function-space priors which, in combination with a likelihood for the observed data $\mathcal{L}(\mathbf{y}|g(\mathbf{x}), \boldsymbol{\sigma})$, where $\mathbf{y}$ is a set of data points with a set of errors $\boldsymbol{\sigma}$, define a regression model. Then, observations can be used to inform the GP posterior (i.e. the statistical properties of the set of random variables) $\mathcal{P}(g(\mathbf{x})|\mathbf{y}, \boldsymbol{\sigma})$, which determines the subset of functions most consistent with the data.

Since the Hubble rate is generally regarded as a monotonically increasing function, it is important to define a non-zero mean for the GP. This prevents the GP from simply fitting the long-range upwards

Table 1. Values of the cosmological parameters used to define the fiducial cosmology. Values based of *Planck* 2018 TTTEEE + lowE cosmology (Planck Collaboration VI 2020).

Parameter	Value
$\overline{\Omega}_{\rm m}$	0.316
$\overline{\Omega}_{\Lambda}$	0.683
$\overline{\Omega}_{\rm r}$	9.24510^{-5}
$\overline{H}_0$	67.27

trend of $H(z)$ while washing out interesting local features (Shafieloo, Kim & Linder 2012). In this paper, we will define the mean of the GP in terms of a fiducial ΛCDM prediction:

$$\overline{H}(z) \equiv \overline{H_0}\sqrt{\overline{\Omega}_m(1+z)^3 + \overline{\Omega}_r(1+z)^4 + \overline{\Omega}_\Lambda}, \tag{8}$$

where $\overline{\Omega}_m$, $\overline{\Omega}_{\rm r}$, and $\overline{\Omega}_\Lambda$ stand for the present values of the cosmological densities of matter, radiation, and dark energy, respectively, as given by the *Planck* 2018 TTTEEE + lowE cosmology (see Table 1). In other words, they are completely fixed and are not variables.

In order to prevent this (ultimately arbitrary) choice of mean from biasing our constraints on the cosmological parameters, we define a free amplitude parameter A_0 that multiplies the mean of the GP such that

$$H_{\rm m}(z) \equiv A_0\,\overline{H}(z). \tag{9}$$

Simply put, if the data are somewhat away from what one might expect from the fiducial ΛCDM background, the GP will have to soak up the large-scale differences, or trends, in detriment to the small-scale, local features. Moreover, in those regions where data are sparse, the GP constraints are highly dominated by their prior, i.e. the chosen mean. If such mean systematically falls beneath or above the data, it can lead to spurious trends in the final results. In Appendix C, we show that these effects can substantially bias the constraints we obtain in the absence of A_0. For these reasons, we advise against common practices such as employing a constant as a mean for a GP modelling the recent expansion history or extrapolating GP results to regions where they become dominated by the choice of mean and covariance function.

The Hubble rate must also be a continuous and smooth function. Therefore, it is important that the covariance function of the GP reflect such properties (Dialektopoulos et al. 2021). Ultimately, we chose a square exponential covariance function to model the correlations between the different nodes of the GP. This decision was made based on the fact that the square exponential is computationally inexpensive and infinitely differentiable kernel appropriate for modelling smooth fluctuations around the mean of the GP. Mathematically, the square exponential covariance function is defined as

$$k\left[g(\boldsymbol{x}), g(\boldsymbol{x}')\right] = \eta^2 \exp\left[\frac{-|g(\boldsymbol{x}) - g(\boldsymbol{x}')|^2}{2l^2}\right], \tag{10}$$

where η is the amplitude of the oscillations around the mean and l is the correlation length between the GP nodes. The parameters η and l are known as hyperparameters since they constrain the possible values that the nodes, i.e. the parameters the GP, can take. In other words, the hyperparameters dictate the family of functions available to the GP. In addition to this, a white noise term with amplitude 10^{-3} was added to the covariance function to ensure numerical stability.

Sampling over GPs is extremely efficient when the model for the observed data is linearly related to the GP and the likelihood is Gaussian. In this case, it can be shown that the posterior distribution also takes the form of a GP for which the mean and covariance functions can be calculated analytically by marginalizing over the nodes of the original GP (Rasmussen & Williams 2006). However, when the observed data are not linearly related to the GP, the posterior distribution becomes non-Gaussian. Thus, each node of the GP, i.e. each dimension of the multivariate Gaussian distribution, must be treated as a newly added degree of freedom in the sampling process (i.e. a new parameter).

Exploring such a vast parameter space is effectively unfeasible with traditional non-gradient-based sampling algorithms and requires more sophisticated samplers. In this work, we employ the No U-turn Sampler (NUTS) (Hoffman & Gelman 2011), a self-tuning variant of Hamiltonian Monte Carlo (HMC) (MacKay 2002; Betancourt 2017), which simulates Hamiltonian trajectories through the parameter space to generate efficient proposal steps. This allows us to handle hundreds or thousands of parameters during the inference process efficiently. We employ the NUTS implementation of the PYTHON package `Pymc3` (Salvatier, Wiecki & Fonnesbeck 2015), which makes use of the tensor package `Theano` (The Theano Development Team et al. 2016) as a back end to build a symbolic graph of the model used to fit the data. This graph is then used to perform automatic differentiation (Margossian 2018) to obtain the gradient of the regression model needed for HMC. Throughout the likelihood, we make use of simple integration schemes, e.g. Runge–Kutta, trapezoidal rule, on which THEANO can apply automatic differentiation to make the likelihood differentiable in all parameters.

In the case of distances (see equation 1), the integral over $1/H_{\mathcal{GP}}$ was performed using the trapezoidal rule with $s \equiv \log(1+z)$ as the integration variable. In the case of the linear growth rate, the system of differential equations shown in equation (6) was solved for $y(s)$ and $D(s)$ employing a second-order Runge–Kutta scheme, integrating over the redshift range $0 < z < 1100$ from the past into the present with initial conditions $D(z = 1100) = a(z = 1100)$ and $y(z = 1100) = a(z = 1100)^3 E(z = 1100)$. Note that these initial conditions are strictly correct only for a purely matter-dominated universe, which is not accurate at $z \sim 1000$. However, the impact of this assumption is negligible by comparison to current uncertainties on growth measurements. In combination, these methods allow us to obtain sub-percentage accuracy throughout the entire redshift range of the GP with respect the output of cosmological CLASS (Lesgourgues 2011), which performs the full numerical calculation.

In order to cover the redshift range $0 < z < 1100$ while keeping the numerical errors under control, we sampled the GP evenly in s as opposed to redshift itself. This variable concentrates most of the GP samples at low redshift where most of our data lay while offering great numerical accuracy (Joudaki et al. 2018). This allowed us to cover our desired redshift range with only 200 nodes, i.e. with a 200-dimensional GP.

In addition to the 200 parameters associated with the GP, we also sample over the cosmological parameters present in equation (3), i.e. $\Omega_{\rm m}$ and σ_8, as well as the GP hyperparameters η and l described in equation (10). We define the GP not over the Hubble rate itself but over as relative deviations from the ΛCDM background

$$H_{\mathcal{GP}} \equiv H_{\rm m}(s)[1 + \delta H_{\mathcal{GP}}(s)],$$

where $\delta H_{\mathcal{GP}}$ is GP centred at zero. This approach has the added benefit of normalizing the amplitude of the oscillations of the GP with respect the mean making the sampling of η far more efficient by virtue of reducing its potential range of values. Note that the correlation length scale l is defined in units of s as opposed to z. We also marginalize over the absolute magnitude of the supernovae M (see Section 3.2 for details), the scale of the sound horizon $r_{\rm s}$, and

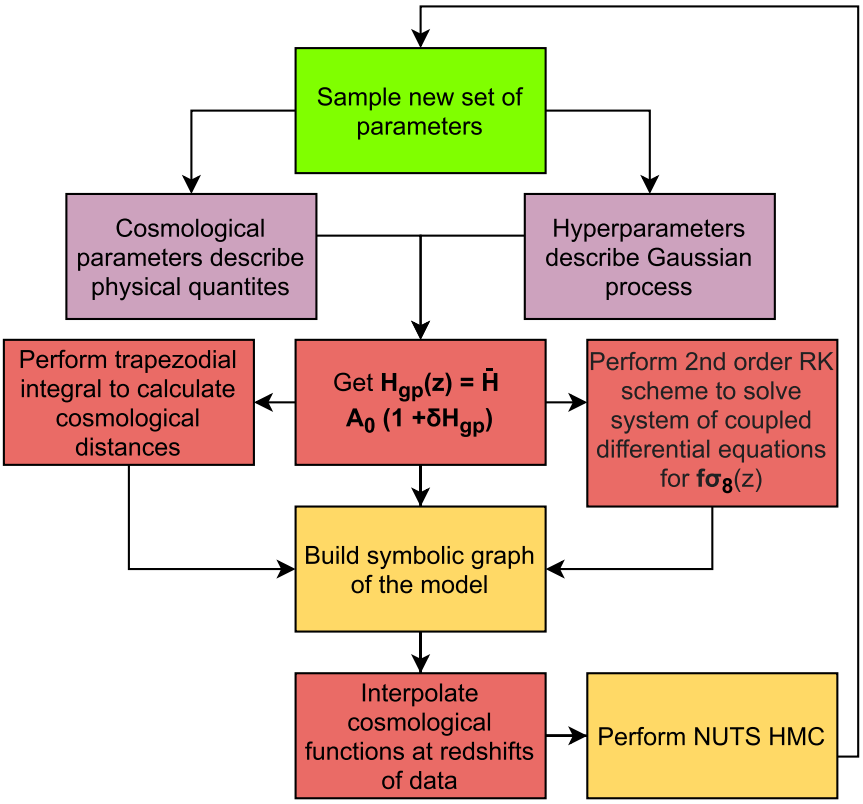

Figure 1. Shows a schematic representation of the data analysis pipeline.

the amplitude of H_m, A_0. A schematic of the model can be found in Fig. 1.

It is important to emphasize that we perform a fully Bayesian inference over the GP, as opposed to what it is known as an empirical Bayesian analysis in which first, the marginal likelihood of the GP hyperparameters is maximized, and then, keeping their values fixed, the conditional posterior over the GP is inferred. While for large sets of data the output of the two approaches converges to the same results, when only sparse data are available, the fact that the empirical Bayesian analysis does not account for the full posterior volume of the hyperparameters can lead to an under-accounting of uncertainties.

In order to establish the reliability of the methodology developed in this work for cosmological inference, and the robustness of the fiducial results, we also considered a series of alternative analyses (see Colgáin & Sheikh-Jabbari 2021, for a discussion of different GP implementations). In the first test, the hyperparameters of the GP (η, l) were kept fixed. We will label results from this analysis as 'Fixed HP'. In the second test, instead of sampling over the A_0 parameter, we performed a two-step analysis. In the first step, a standard ΛCDM model was fit to the data. Based on this best-fitting ΛCDM model, an expansion history was derived. Then, in the second step, the best-fitting expansion history was used as the mean of the GP during the analysis while fixing $A_0 = 1$. We will label results from this analysis as 'Two-Steps'.

A summary of the priors used in the fiducial and alternative analyses can be found in Table 2. As a general rule, when performing Bayesian inference one should avoid broad, uniform priors (Gelman, Simpson & Betancourt 2017). This is mainly due to the fact that they do not accurately represent the prior knowledge, put a lot of posterior mass in unlikely values, and introduce hard boundaries that can be difficult to motivate. This last consideration is particularly important

Table 2. Sampled parameters and their priors in the standard analysis (first column), the fixed hyperparameters analysis (second column), and the Two-Steps analysis (third column).

Parameter	Fiducial	Fixed HP	Two-Steps
η	$\mathcal{N}_{1/2}(0, 0.2)$	0.2	$\mathcal{N}_{1/2}(0, 0.2)$
l	$U(0.01, 6)$	1.0	$U(0.01, 6)$
Ω_m	$U(0, 1)$	$U(0, 1)$	$U(0, 1)$
σ_8	$\mathcal{N}(0.8, 0.5)$	$\mathcal{N}(0.8, 0.5)$	$\mathcal{N}(0.8, 0.5)$
A_0	$U(0.8, 1.2)$	$U(0.8, 1.2)$	1
M	$\mathcal{N}(-19.2, 1)$	$\mathcal{N}(-19.2, 1)$	$\mathcal{N}(-19.2, 1)$
r_s	$\mathcal{N}(150, 5)$	$\mathcal{N}(150, 5)$	$\mathcal{N}(150, 5)$

when using HMC since sharp edges in parameter space can lead to the sampling process becoming inefficient. Following this principle, we employed a half-Gaussian distribution with zero mean and standard deviation 0.2 as prior distribution for the hyperparameter η to down-weight extreme deviations [i.e. 20 per cent and above, well within the observational errors on $H(z)$] from the chosen GP mean without introducing any unnecessary hard boundaries. In the case of l, we used a uniform distribution between $0.01 < l < 6$ for the following reasons. First, there is no reason to down-weight long correlation modes against short ones or vice versa. Secondly, looking at equation (10), it is possible to see that as $l \to 0$, the value of the covariance function approaches zero regardless of the value of η. This opens a vast volume in the parameter space, which can lead to an inefficient sampling. Thirdly, the likelihood function becomes flat at such small scales since there is no information in the data to constrain those small-scale modes. Fourthly, the expansion rate is expected to have some degree of temporal correlations, and therefore the limit $l =$

0 must be excluded. The parameter $\Omega_{\rm m}$ was sampled from a uniform distribution between 0 and 1 to enforce the physical boundaries on the allowed values for the cosmological matter fraction. In the case of σ_8 for which there is no physically motivated upper limit, we employ a better behaved Gaussian prior centred at 0.8 and with 0.5 standard deviation. Given the degeneracy of A_0 with the GP parameters, the parameter was sampled from a uniform distribution between 0.8 and 1.2, which amply encompasses the current discrepancy in H_0 between CMB data and local measurements. The supernova absolute magnitude parameter M was sampled from a Gaussian distribution centred at value found by the SH0ES collaboration for the parameter $M = -19.2$, with a standard deviation of 1. While the mean value corresponds to a local expansion rate of $H_0 \simeq 74.0$ km s^{-1} Mpc^{-1}, the standard deviation ensures that all values in the range $50 < H_0 < 100$ km s^{-1} Mpc^{-1} fall within the 1σ region of the prior distribution. Finally, the sound horizon scale, $r_{\rm s}$, was sampled from a Gaussian distribution centred at 150 Mpc with a standard deviation of 5 Mpc. We do this instead of computing $r_{\rm s}$ from the expansion history in combination with a Big Bang Nucleosynthesis (BBN) prior to allow for largest deviations from the fiducial cosmology. This was needed to recover the test cosmologies of Appendix C.

3 OBSERVABLES AND DATA SETS

In order to make the most of the modelling freedom offered by GPs, we consider as much data as possible. In this work, we use a combination of several different probes that together account for 91 data points for a variety of cosmological observables. A summary of the data used in this work can be found in Table 3 and Fig. 2.

3.1 Cosmic chronometers

Cosmic chronometers (CCs) are tracers of the evolution of the differential age of the Universe as a function of redshift. Since $H(z) \equiv \dot{a}/a = -(dt/dz)/(1+z)$, a measurement of dt/dz directly yields the expansion rate (Jimenez & Loeb 2002). By measuring the age difference between two ensembles of passively evolving galaxies at different redshifts, one can determine the derivative of redshift with respect to cosmic time, dz/dt. Massive, early, passively evolving galaxies have been found to be very good tracers in this sense (Cimatti, Daddi & Renzini 2006; Thomas et al. 2011; Moresco 2015; Moresco et al. 2018, 2020) and have been used extensively over the past two decades to measure $H(z)$ up to $z \approx 2$. In this work, we make use of the $H(z)$ measurements from CCs summarized in table 1 of Vagnozzi et al. (2021).

3.2 Supernovae

Type Ia supernovae (SNe Ia) – titanic explosions of white dwarfs in multistar systems (Hoyle & Fowler 1960; Colgate & McKee 1969) – are highly prized observations in cosmology due to their capacity to act as standard candles (Phillips et al. 1999; Freedman et al. 2001).

However, SNe Ia by themselves can only inform their relative distance to one another and need to be calibrated with nearby SNe Ia of known redshift and luminosity distance $D_{\rm L}$ to obtain absolute distances. Thus, SNe Ia inform the relationship

$$\mu(z) = 5\log_{10} D_{\rm L}(z) + 25 + M, \tag{11}$$

known as the luminosity distance modulus where M is the calibrator known as the absolute magnitude of the SNe Ia. Therefore, once M has been determined, SNe Ia luminosity distance measurements can be used to inform the Hubble rate.

In this work, we fit the compressed data vector of the Pantheon sample, known as 'DS17', composed of 40 measurements of the distance modulus (See equation 11) in the range $0.15 \leq z \leq 1.615$ (Scolnic et al. 2018). The original Pantheon sample is composed of the optical light curves and redshifts for 365 spectroscopically confirmed SNe Ia discovered by the Pan-STARRS1 (PS1) Medium Deep Survey combined with the subset of 279 PS1 SN Ia ($0.03 < z < 0.68$) with useful distance estimates of SN Ia from SDSS, SNLS, various low-z, and *HST* samples to form the largest combined sample of SN Ia consisting of a total of 1048 SN Ia ranging from $0.01 < z < 2.3$ (Scolnic et al. 2018).

In the light of recent works in the literature questioning the accuracy of the absolute calibration of important sectors of Pantheon sample (Shah, Lemos & Lahav 2021), we marginalize over the absolute magnitude of the supernovae as opposed to fixing its value. Due to the degeneracy between M and H_0, this is equivalent to fitting the expansion rate, $E(z) = H(z)/H_0$, as opposed to the Hubble rate, $H(z)$.

3.3 Baryon acoustic oscillations

Baryon acoustic oscillations (BAOs) enhance matter overdensities at a characteristic physical separation scale, which corresponds to the size of the sound horizon at the end of the drag epoch, $r_{\rm s}(z_{\rm d})$ (Peebles & Yu 1970; Hu & Dodelson 2002). The sound horizon is defined as the distance a pressure wave can travel from its time of emission in the very early Universe up to a given redshift. This can be expressed as

$$r_{\rm s}(z) = \int_z^\infty \frac{c_{\rm s}\,{\rm d}z'}{H(z')}, \tag{12}$$

where $c_{\rm s}$ denotes the speed of sound, and where $H(z)$ is the expansion rate at redshift z. The end of the drag epoch is defined as the time when photon pressure can no longer prevent gravitational instability in baryons around $z \sim 1020$ (Komatsu et al. 2009).

The BAO feature can be measured in the directions parallel and perpendicular to the line of sight. Perpendicular to the line of sight, the BAO feature informs the trigonometric relationship

$$\theta = \frac{r_{\rm s}(z_{\rm d})}{D_M(z)}, \tag{13}$$

where θ is the angle under which the scale of the sound horizon is observed. Parallel to the line of sight, the BAO feature informs the relationship $\Delta z = H(z) r_{\rm s}(z_{\rm d})$, which can be used to constrain the expansion history of the Universe directly.

In this work, we make use of the 12th data release of the galaxy clustering data set of the Baryon Oscillation Spectroscopic Survey (BOSS DR12), which forms part of the Sloan Digital Sky Survey (SDSS) III. BOSS DR12 comprises 1.2 million galaxies over an area of 9329 deg^2 and volume of 18.7 Gpc^3, divided into three partially overlapping redshift slices centred at effective redshifts 0.38, 0.51, and 0.61.

We fit the Alcock–Paczynski parameters $\alpha_\parallel$ and $\alpha_\perp$ as reported by the BOSS DR12 data products

$$\frac{[H(z)]_{\rm fid}}{\alpha_\parallel} = \frac{H(z)[r_{\rm s}(z_{\rm d})]_{\rm fid}}{r_{\rm s}(z_{\rm d})}, \quad \alpha_\perp [\chi(z)]_{\rm fid} = \frac{\chi / r_{\rm s}(z_{\rm d})}{[r_{\rm s}(z_{\rm d})]_{\rm fid}}, \tag{14}$$

from the reconstruction of the BAO feature at the three different redshift bins where $[r_{\rm s}(z_{\rm d})]_{\rm fid} = 147.78$ Mpc is the scale of the sound horizon at drag epoch as given by the fiducial cosmology used for the reconstruction. $[H(z)]_{\rm fid}$ and $[\chi(z)]_{\rm fid}$ are the corresponding Hubble

Table 3. Data sets used in our analysis, listing the probe, the redshift range of the probe, the choice of observable, and the size of the data vector. See Fig. 2 for a pictorial representation.

Data set	Probe	Redshifts	Observable			Data points
			$H(z)$	$D_M(z)$	$f\sigma_8$	
CCs (Vagnozzi et al. 2021)	Cosmic chronometers	0.07–2.36	✓	×	×	35
Pantheon DS17(Scolnic et al. 2018)	SNe Ia	0.38–0.61	×	✓	×	40
BOSS DR12 (Alam et al. 2017)	BAO + RSD	0.38–0.61	✓	✓	✓	3 × 3
eBOSS DR16 (Alam et al. 2021)	BAO + RSD	1.48	✓	×	×	1 × 3
Wigglez (Blake et al. 2012)	RSD	0.44–0.73	×	×	✓	1 × 3
DSS (Stahl et al. 2021)	RSD	0	×	×	✓	1
Planck 2018 (Planck Collaboration VI 2020)	CMB	1090.30	×	✓	×	1
DESI (Font-Ribera et al. 2014)	BAO + RSD	0.15–1.85	✓	✓	✓	3 × 18

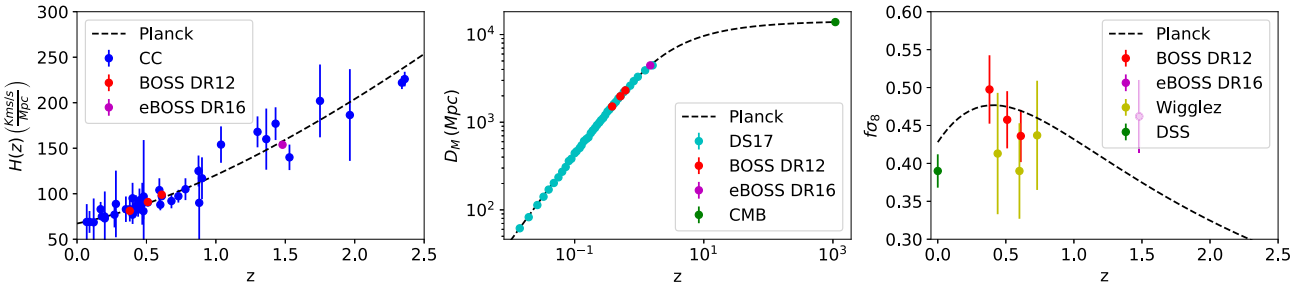

Figure 2. Data points from the different surveys used in this work across redshift for the three cosmological functions of interest $H(z)$, $D_{\rm M}$, and $f\sigma_8$.

parameter and comoving radial distance for the fiducial cosmology, respectively.

In addition to this, we employ the anisotropic clustering of quasars in the 16th data release of the extended Baryon Oscillation Spectroscopic Survey (eBOSS DR16 Blanton et al. 2017), which forms part of the Sloan Digital Sky Survey (SDSS) IV (Dawson et al. 2016). The eBOSS DR16 catalogue contains 343 708 quasars between $0.8 < z < 2.2$, from which BAO and RSD measurements are obtained at an effective redshift of $z_{\rm eff} = 1.48$ (Hou et al. 2021). We use the results from the configuration space analysis performed by measuring the two-point correlation function and decomposing it using the Legendre polynomials. Similar to BOSS DR12, the BAO signal is measured both parallel and perpendicular to the line of sight. This allows for the measurement of the geometrical relationships $D_{\rm H}(z_{\rm eff})/[r_{\rm d}]_{\rm fid}$ and $D_{\rm M}(z_{\rm eff})/[r_{\rm d}]_{\rm fid}$, respectively, where $D_{\rm H}(z) \equiv c/H(z)$ and $[r_{\rm d}]_{\rm fid} = 147.3$.

Finally, we make use of the *Planck* 2018 measurement of the BAO angular scale $\theta_* = \frac{D_{\rm A}(z_*)}{r_{\rm s}(z_*)}$, where $z_* \sim 1100$ is the redshift of the last scattering surface. We use the *Planck* measurement from the temperature and polarization maps denoted as TTTEEE + lowE.

3.4 Redshift space distortions

Redshift space distortions (RSDs) are modifications to the observed redshift of a given object caused by its radial peculiar velocity (Kaiser 1987). RSDs are caused by deviations from the Hubble flow that are gravitationally induced by inhomogeneities in the gravitational potential of the surrounding matter distribution. On large, linear scales, RSDs are dominated by the infall towards overdense structures, known as the Kaiser effect (Hamilton 1998). Clustering two-point statistics as a function of transverse and line-of-sight separation are sensitive to the quantity $f\sigma_8$ via RSDs (Beutler et al. 2017). Alternatively, SNe Ia themselves can be used as a probe of the local velocity field (Riess 2000; Tully, Courtois & Sorce 2016; Stahl et al. 2021), which can also be used to measure this parameter.

We use the three measurements of $f\sigma_8(z)$ from RSD from the BOSS DR12 data, obtained using the anisotropic clustering of the pre-reconstruction density field (Alam et al. 2017). We also include the value of $f\sigma_8(z_{\rm eff})$ measured from the BOSS DR16 quasar sample. The BAO and RSD measurements of both data sets are extracted from the same set of observations. As such, they are not statistically independent, and we account for their full covariance matrix in our analysis (Alam et al. 2017; Hou et al. 2021). In addition to these, we use the $f\sigma_8$ measurements reported by the WiggleZ Dark Energy Survey at the Australian Astronomical Observatory (Drinkwater et al. 2010) at redshifts 0.44, 0.60, and 0.73.

Finally, we also use the value of $f\sigma_8(z = 0)$ derived from the measured peculiar velocities of the Democratic Samples of Supernovae (DSS, Stahl et al. 2021), the largest catalogue used to study bulk flows in the nearby Universe, compiled of 775 low-redshift Type Ia and II supernovae (SNe Ia & II).

3.5 Synthetic stage-IV data

In addition to the previously discussed observables and data sets, we also produce forecasts for future experiments, focusing on the Dark Energy Spectroscopic Instrument (DESI). DESI is a galaxy and quasar redshift survey currently taking data from the Mayall 4-meter telescope at Kitt Peak National Observatory. The baseline area is 14 000 sq. deg. We use the forecast errors for the measurements of the Hubble rate, $H(z)$; the angular diameter distance, $D_{\rm A}(z)$; and the growth rate measurement $f\sigma_8$ reported by Font-Ribera et al. (2014) to create a set synthetic measurements for $H(z)$, $D_A(z)$, and $f\sigma_8$ at an array of 18 redshifts from 0.15 to 1.85. The synthetic measurements were generated using the best-fitting *Planck* 2018 cosmology, including measurement noise following the statistical uncertainties reported by Font-Ribera et al. (2014).

4 RESULTS

In this section, we present the results of our analysis, including both the constraints on expansion history and cosmological parameters from current data, and forecasts for ongoing and future surveys.

4.1 Validity of the methodology

Before discussing the results of our analysis, we must first verify its reliability. Our methodology produces two types of results: constraints on the GP used to model the expansion history and on the cosmological parameters (mainly Ω_M) involved in solving the Jeans equation (equation 3). We thus report results on both aspects. In Appendix B, we present the results of the alternative analyses described at the end of Section 2 and show that, despite the different treatments of the GP, they produce statistically compatible constraints for the cosmological functions as well as for the cosmological parameters and similar uncertainties on both. In Appendix C, we considered five different cosmologies, each progressively more discrepant with our fiducial cosmology (*Planck* 2018), and generated mock data based on each them. We then showed that our methodology recovers the input cosmologies within statistical uncertainty. In addition to this, in Appendix D, we discuss the specific NUTS setup used to produce our results. These settings allow us to achieve a Gelman–Rubin convergence test (Gelman & Rubin 1992) value of $R - 1 < 0.01$ for all the combinations of data considered.

4.2 Current constraints

4.2.1 Cosmological functions

Before presenting the results for the cosmological functions of interest, i.e. the expansion history $H(s)$ and linear growth rate $f\sigma_8$, we must first discuss the results on the core of our analysis, the GP on $\delta H(s)$. We found that our analysis of current data produces $\delta H(s)$ constraints compatible with 0 at all redshifts at less than 1σ deviation. This means that the mean of the GP, $H_m(s) = A_0\overline{H}(s)$, is capable of capturing the long-range correlations of the data allowing the GP to fit local features. The recovered bounds on δH are shown in Fig. 3.

Moreover, we quantified how well different combinations of data can constrain $\delta H(s)$. In other words, we measured how strong the agreement of $\delta H(s)$ with zero is, and how it is affected by the data considered and the analysis choices. However, the fact that $\delta H(s)$ has a multivariate distribution means that there is no unique figure of merit for how well data constrain it. In this work, we focused in two numbers. On the one hand, we looked at the hyperparameter η that constrains the prior distribution of values that $\delta H(s)$ can take. On the other hand, we computed the mean variance of the $\delta H(s)$ samples across redshift. In other words, for each parameter of $\delta H(s)$ (i.e. $\{\delta H(s_1),\ \delta H(s_2),\ ...,\ \delta H(s_{200})\}$), we computed the variance of the HMC samples. Then, we took mean value of those variances, which is equivalent to averaging over redshift. We refer to this statistic as $\overline{\sigma}(\delta H(s))$. The motivation behind $\overline{\sigma}(\delta H(s))$ lies in the fact that it directly translates to average fractional constraints on $H(z)$ that can be readily interpreted.

A summary of the impact of the different data sets and analysis choices on the distribution of η and $\overline{\sigma}(\delta H(s))$ can be found in Table 4. For the combination of data sets employed in our fiducial analysis, we find $\eta = 0.113 \pm 0.075$ and an $\overline{\sigma}(\delta H(s)) = 0.094 \pm 0.004$ corresponding to an average 9.4 ± 0.4 per cent constraint on $H(z)$ across redshift. Removing the CMB data point significantly wors-

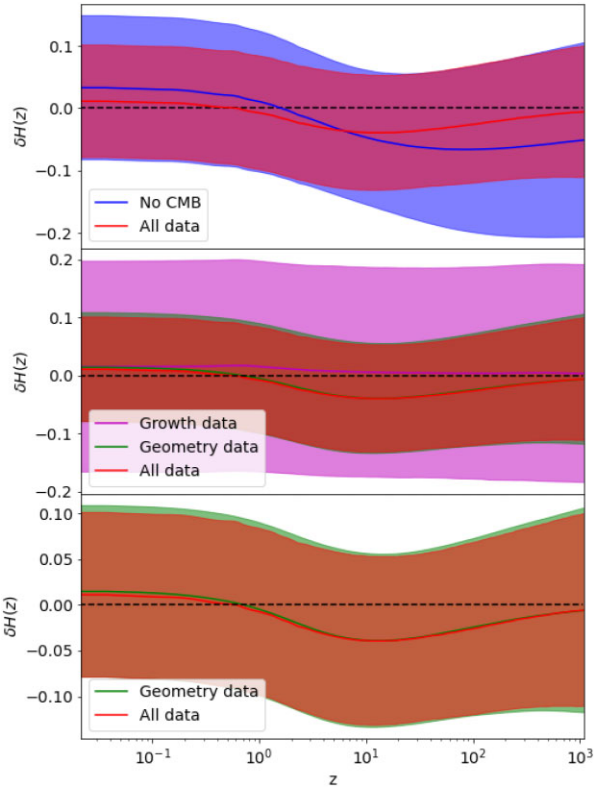

Figure 3. 1σ-constraints on $\delta H(z)$ broken down by type of data considered. Solid lines represent the mean of the GPs at each redshift. In red, we display the constraints resulting from the analysis of all present data; in blue, the effect of removing the CMB data set; in black, the effect of fixing the Ω_m and σ_8 to their best-fitting (BF) value; in magenta, the constraints resulting of considering only growth data; and in green, the constraints resulting of considering only geometry data.

Table 4. One-dimensional constraints on the hyperparameter η (first column) and the mean variance of $\delta H(z)$ (second column) for different analyses.

Analysis	η	$\overline{\sigma}(\delta H(s))$
All data (ΛCDM)	0 ± 0	0.011 ± 0.003
DESI + CMB (ΛCDM)	0 ± 0	0.002 ± 0.001
All data	0.113 ± 0.075	0.094 ± 0.004
All data (fixed HP)	0.2	0.2
All data (Two-Steps)	0.044 ± 0.039	0.025 ± 0.01
No CMB	0.142 ± 0.096	0.125 ± 0.016
No DSS	0.111 ± 0.074	0.091 ± 0.005
Growth data	0.147 ± 0.114	0.183 ± 0.003
Geometry data	0.122 ± 0.077	0.098 ± 0.005
DESI + CMB	0.085 ± 0.074	0.08 ± 0.004

ened both constraints finding $\eta = 0.142 \pm 0.096$ and an average 12.5 ± 1.6 per cent constraint on $H(z)$ across redshift. In order to better understand this effect, we can look at the first panel in Fig. 3. In this figure, we can observe how removing the CMB data from the analysis significantly widens the constraints of the GP, specially beyond $z > 2.5$ (see Table 4). This is to be expected as the CMB data are the only point we have above $z = 2.5$. Thus, the constraints from this integrated effect are expected to become dominant in the redshift range between $2.5 < z < 1100$. However, it is important to note that the CMB is not the only contributor to the $\delta H(s)$ constraints over this redshift range since $f\sigma_8$ data also constrain $\delta H(s)$ over its

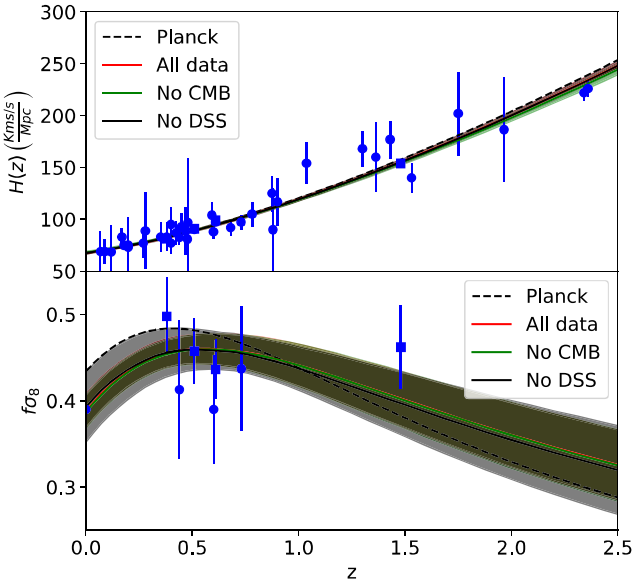

Figure 4. 1σ constraints for the cosmological functions $H(z)$ and $f\sigma_8$ (top and bottom panels, respectively) broken down by combination of data set. Solid lines represent the mean of the GPs at each redshift. The dashed black lines show the prediction for each cosmological function using our *Planck* 2018 fiducial cosmology (see Table 1). In red, we show the constraints resulting of the analysis of all present data; in green, the impact of removing the CMB data set; and in black, the impact of removing the DSS data set.

whole domain through its role in solving the Jeans equation. The associated constraint is, however, very weak.

For the purpose of studying the effect of different data types, we split the data points within the data sets employed in the fiducial analysis in two groups: 'geometry' – exclusively containing measurements of the expansion history – and 'growth' – solely containing $f\sigma_8$ measurements.

As we can see in the second panel of Fig. 3, only growth data are much weaker at constraining $\delta H(z)$. From Table 4, we see that constraints from growth data alone on $\overline{\sigma}(\delta H(s))$ are approximately twice as wide as those resulting from analysing the entire data set. These constraints are consistent with the prior on the hyperparameter η. On the other hand, the constraining power of the geometry data is only slightly weaker than that of the entire data set. Hence, the $\delta H(z)$ constraints are mostly dominated by the geometry data sets as one would expect. None the less, the addition of growth data increases constraining power. This is shown explicitly in the last panel of Fig. 3, which shows the results of using geometry data alone compared to those using the full data set. This recovers the expected behaviour: more data increase the constraining power and the contours shrink.

We now shift the focus of our discussion to the constraints we derive from $\delta H(s)$ for the expansion history itself, $H(z)$, and the linear growth of matter anisotropies, $f\sigma_8$. Comparing the constraints for both cosmological functions from our analysis of current data with the *Planck* 2018 predictions, we find an overall good agreement, finding both functions to contain the *Planck* 2018 predictions within their 2σ confidence contours. This can be seen in Fig. 4. None the less, two remarks can be made. First, we observed a greater than 1σ preference for a lower $f\sigma_8$ between $0 < z < 0.75$, mostly driven by the DSS data point. However, the constraining power of current $f\sigma_8$ data is too weak to make a case for the presence of new physics. Secondly, our model-independent analysis finds the supernova absolute magnitude parameter to be $M = -19.43 \pm 0.026$, a constraint which is in 5σ tension with the SHOES preferred value (Efstathiou 2021). However, this is not surprising, given the known tension between the data sets used to inform the GP reconstruction.

4.2.2 *Cosmological parameters*

We now focus on the constraints on the specific cosmological parameters Ω_M and σ_8. We will also show constraints on the derived parameter $S_8 = \sigma_8\sqrt{\Omega_m/0.3}$ and on the local value of the expansion rate, given in our case by $H_0 \equiv A_0\,\overline{H}_0\,(1 + \delta H(s = 0))$. A summary of the constraints obtained by the different analyses considered in this work can be found in Table 5 with a graphical illustration in Fig 5. Full two-dimensional (2D) contours for the respective sets of constraints, including hyperparameters, can be found in Appendix A. We primarily focus our discussion on the cosmological parameter Ω_m, the only remaining degree of freedom in equation (3).

To establish a benchmark against which to compare our method, we start by examining the constraints obtained assuming a ΛCDM model in which we vary H_0, Ω_m, and σ_8. This allows us to quantify the impact of performing a model-independent analysis using GPs on the final constraining power. Looking at Fig. 5 and Table 5, we can observe that assuming ΛCDM, $\Omega_m = 0.283 \pm 0.007$. In other words, for the setup used in this work, we can constrain Ω_m to around 2 per cent precision if we undertake a model-dependent analysis with ΛCDM. In this case, Ω_m receives information from both background and perturbations.

In turn, our fiducial model-independent analysis yields $\Omega_m = 0.224 \pm 0.066$, inflating the uncertainty by a factor of $\sim$9. Comparing this result with the *Planck* 2018, $\Omega_m = 0.317 \pm 0.008$, our Ω_m constraint is lower but statistically compatible with the *Planck* 2018 constraint and our ΛCDM analysis both at 1.5σ.

Table 5. Constraints on the cosmological parameters Ω_m, σ_8, S_8, and H_0 (first to fourth columns, respectively) for each of the different analyses (rows), as well as the *Planck* 2018 constraints and ΛCDM analyses of current and DESI + CMB for reference (first to third rows, respectively).

Analysis	Ω_m	σ_8	S_8	$H_0 = \bar{H}_0 A_0(1 + \delta H(0))$
Planck 2018	0.317 ± 0.008	0.812 ± 0.007	0.834 ± 0.016	67.27 ± 0.006
All data (ΛCDM)	0.283 ± 0.007	0.8 ± 0.029	0.777 ± 0.028	68.601 ± 0.775
DESI + CMB (ΛCDM)	0.316 ± 0.006	0.812 ± 0.003	0.834 ± 0.008	66.992 ± 0.311
All data	0.224 ± 0.066	0.946 ± 0.158	0.788 ± 0.029	67.715 ± 0.93
All data (fixed HP)	0.228 ± 0.067	0.932 ± 0.155	0.785 ± 0.03	68.113 ± 1.061
All data (Two-Steps)	0.226 ± 0.066	0.936 ± 0.151	0.787 ± 0.029	68.144 ± 0.718
No CMB	0.227 ± 0.068	0.936 ± 0.156	0.786 ± 0.03	67.94 ± 1.034
No DSS	0.229 ± 0.106	0.974 ± 0.218	0.791 ± 0.047	67.766 ± 0.96
DESI + CMB	0.293 ± 0.013	0.839 ± 0.014	0.828 ± 0.008	66.788 ± 0.371

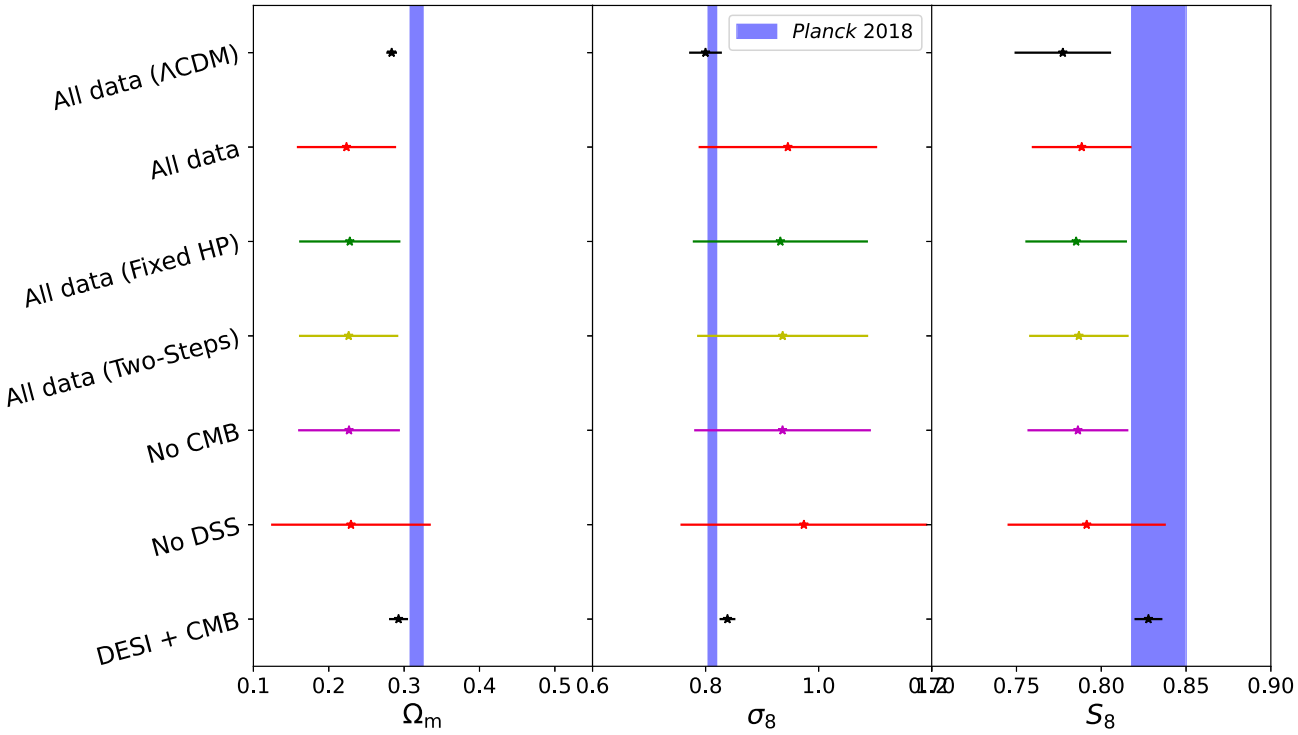

Figure 5. Comparison between the different 1σ constraints for the cosmological parameters S_8, σ_8, and Ω_m (first, second, and third panels, respectively). In each panel, the *Planck* 2018 constraint is displayed in the form of a blue band for comparison.

Looking at the relevance of the different individual data sets on the constraints, we observe an excellent agreement between all the different combinations considered (see Fig. 5 and Table 5). Removing the DSS data, one of the most precise $f\sigma_8$ measurements, significantly worsens the Ω_m constraints by nearly 60 per cent. On the other hand, removing the CMB data set resulted in nearly identical constraints for the cosmological parameters. This is due to the fact that, in the presence of other geometry data to inform the expansion history, Ω_m constraints become dominated by growth data through the relationship between both. Thus, it is fair to ask what the impact of completely removing any type of geometry data from the analysis is. Analytically, we can see from equation (4) that in the presence of measurements of the linear growth rate and an arbitrary value of Ω_m, one can always find an expansion history that solves the differential equation. This degeneracy between the expansion history and Ω_m in equation (4) prevents our methodology from obtaining any meaningful constraints on Ω_m in the absence of Geometry data that are not completely dominated by our choice of GP mean and hyperparameter priors.

Looking at the parameters σ_8 and S_8 in more detail, we found compatible constraints with the *Planck* 2018 cosmology up to 1σ. However, it is worth mentioning that our results show a mild tendency towards higher σ_8 values which, combined with the tendency towards lower Ω_m values, results in lower S_8 values. This is consistent with the underprediction of $f\sigma_8$ between $0 < z < 0.75$ we discussed in the previous section. A lower value of S_8 would also be consistent with the most recent measurements by large-scale structure experiments (DES Collaboration 2021; García-García et al. 2021; Heymans et al. 2021; Krolewski, Ferraro & White 2021; White et al. 2021), the origin of which could lie on a lower value of Ω_m (Hang et al. 2021).

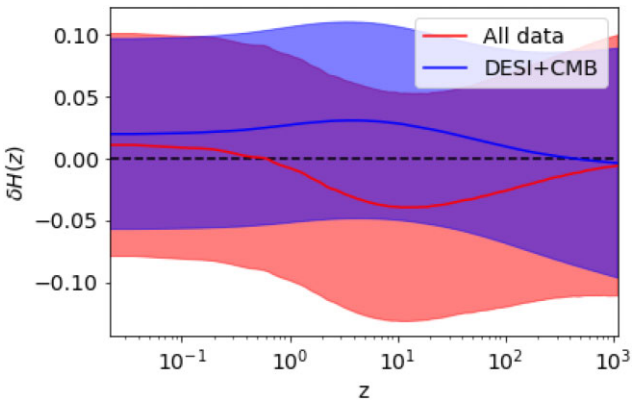

Figure 6. Forecast 1σ-constraints on $\delta H(z)$ from DESI (blue) and using current data (red). Solid lines represent the mean of the GPs at each redshift.

4.3 Forecasts

Our model-independent analysis leads to far weaker constraints than assuming the ΛCDM model. Being data-driven, the performance of the method used here may improve significantly with the advent of next-generation surveys with significantly tighter uncertainties. To quantify this, we repeated our fiducial analysis pipeline on mock data generated based on the forecasted errors for the DESI mission (Font-Ribera et al. 2014) in combination with the *Planck* measurement of θ_*. The results can be found in Fig. 6. In this figure, we can observe a 10 per cent improvement between the expected $\delta H(z)$ constraints from DESI with respect to those of current data. The corresponding η and $\overline{\sigma}(\delta H(s))$ constraints (shown in Table 4) improve by approximately 15 per cent: $\eta = 0.085 \pm 0.074$

and $\overline{\sigma}(\delta H(s)) = 0.080 \pm 0.004$. Looking at the cosmological parameters, DESI (Font-Ribera et al. 2014) in combination with the CMB data set results in nearly five times tighter $\Omega_{\rm m}$ constraints and 10 times better constraints on σ_8.

While these constraints are still significantly worse than the *Planck* 2018 results, they are comparable if not better than using the ΛCDM model to analyse the currently available data used in this work. For example, while GP constraints on $\Omega_{\rm m}$ from DESI are two times wider than those currently found assuming a ΛCDM model, the constraints on σ_8 and S_8 are 2.3 and 3.6 times tighter, respectively.

If we, instead, compare how a model-independent analysis of DESI data using this methodology will pitch against a ΛCDM analysis, we find that the gap between the model-independent and model-dependent constraints shrinks. This can be seen in the fact that, with current data, the ΛCDM constraint on $\Omega_{\rm m}$ is 9.2 times tighter than the one obtained with our methodology. However, in our DESI forecast, it is only twice as good. Similarly, the improvement for the parameter σ_8 reduces from five times tighter constraints to about four times. Our understanding is that, as better data allow us to better reconstruct $H(z)$, the difference between the reconstructed and model-dependent $H(z)$ shrinks, as long as the assumed model fits the data well. As a consequence, the constraints on the other parameters ($\Omega_{\rm m}$, σ_8, and S_8) become more similar. Thus, we expect that in the future, as the quality of the data keeps improving, cosmological constraints from model-independent methodologies, such the one proposed in this work, will rival model-dependent ones.

5 CONCLUSIONS

In this work, we have developed a method to obtain constraints on $H(z)$ and $\Omega_{\rm m}$ purely based on the relationship between the expansion history and the linear growth rate. In order to do so, we employ a GP to model the evolution of the expansion history from present time to recombination.

From this expansion history, we have derived predictions for the comoving distance and the linear growth rate $f\sigma_8$ making use of the physical relationships between the three quantities. Constraints for ΛCDM parameters were obtained by simultaneously fitting a suite of the latest measurements of these three cosmological functions. The data combination used for our fiducial analysis consisted of CCs, the Pantheon supernova catalogue, BAO and RSD data, peculiar velocity data from supernovae, and the position of the first acoustic peak in the CMB power spectrum. Moreover, we also obtained forecast constraints on these cosmological functions from the future DESI data.

Current data can constrain the $H(z)$ GP at an average 9.4 per cent throughout all redshifts. These constraints are compatible up to 1σ with the best-fitting *Planck* 2018 expansion history across $0 < z < 1100$. Our constraints on the expansion rate $f\sigma_8$ lie below the corresponding *Planck* prediction by less than 2σ in the range $0 < z < 0.75$ (a result driven by the Democratic Supernova Sample data).

Translating the GP constraints into constraints of cosmological parameters, we find a model-independent measurement of $\Omega_{\rm m} = 0.224 \pm 0.066$. This result is lower than, but statically compatible with, the *Planck* 2018 (Planck Collaboration VI 2020) cosmology. We also find $S_8 = 0.788 \pm 0.029$, an intermediate value, statistically compatible with both the *Planck* 2018 cosmology (Planck Collaboration VI 2020) and the recent local measurements from weak lensing and galaxy clustering (DES Collaboration 2021; García-García et al. 2021; Heymans et al. 2021; Krolewski et al. 2021; White et al. 2021).

The forecast analysis performed using the methodology of this work predicts that combining the DESI measurements with the CMB BAO data used in this work will yield 15 per cent tighter constraints on $H(z)$ across redshift as well as five times tighter constraints on $\Omega_{\rm m}$. While these constraints are still significantly looser than the model-dependent cosmological constraints of *Planck* 2018, we show that a model-independent analysis of DESI plus CMB BAO data would be as powerful as a ΛCDM analysis of current data. Indeed, we find that model-independent constraints using this methodology would achieve four times tighter S_8 constraints. Thus, in the future it will be possible to weigh in on the ongoing S_8 tension making use of model-independent methods. Moreover, we also show that, as the quality of the data increases as we go into the future, the gap between the constraining power of model-independent and model-dependent constraints will significantly shrink.

Future implementations of this methodology could explore several possible extensions. On the one hand, the types of data used in this work are greatly limited by lack of differentiable tools to obtain theoretical predictions for observables with greater constraining power. The development of tools such as differentiable Boltzmann codes, differentiable emulators of the non-linear matter power spectrum, or differentiable Limber integrators would allow us to fit the power spectrum data directly. These developments would enable model-agnostic analyses similar to that of García-García et al. (2021) but with a greatly reduced number of assumptions and a more reliable measure of uncertainty in their results. On the other hand, it would also be possible to explore the use of GPs to constrain general forms of modified gravity, generalizing works such as Raveri et al. (2017), Espejo et al. (2019), Park, Raveri & Jain (2021), Raveri et al. (2021), and Pogosian et al. (2021), and study how these theories can be informed by the relationship between background and perturbations. Gaussian processes are an exceptional tool to constrain modified gravity since they do not require assuming a particular parametrization of such deviations. A comprehensive list of different departures from ΛCDM that could be explored with a similar methodology to the one presented in this work can be found in Baker, Ferreira & Skordis (2014). Alternatively, one could consider comparing the performance of GPs against other popular tools for non-parametric cosmology such as genetic algorithms (Nesseris 2011; Rajpaul 2012) or neuronal networks (Gómez-Vargas et al. 2021). The convenience of using GPs lies in that they naturally provide easily interpretable information on both the reconstructed function and its posterior uncertainties.

ACKNOWLEDGEMENTS

Author contributions: All authors contributed to the development and writing of this paper. We acknowledge support from the Beecroft Trust. CGG and PGF acknowledge funding from the European Research Council (ERC) under the European Union's Horizon 2020 research and innovation programme (grant agreement no. 693024). DA acknowledges support from the Science and Technology Facilities Council through an Ernest Rutherford Fellowship, grant reference ST/P004474. JRZ is supported by an STFC doctoral studentship.

The analysis made use of the software tools SCIPY (Virtanen et al. 2020), NUMPY (Harris et al. 2020), MATPLOTLIB (Harris et al. 2020), CLASS (Lesgourgues 2011), and GETDIST (Lewis 2019).

Based on observations obtained with *Planck* (http://www.esa.int/Planck), an ESA science mission with instruments and contributions directly funded by ESA member states, NASA, and Canada.

Funding for the Sloan Digital Sky Survey IV has been provided by the Alfred P. Sloan Foundation, the U.S. Department of Energy Office of Science, and the Participating Institutions. SDSS-IV acknowl-

edges support and resources from the Center for High Performance Computing at the University of Utah. The SDSS website can be found at www.sdss.org. SDSS-IV is managed by the Astrophysical Research Consortium for the Participating Institutions of the SDSS Collaboration including the Brazilian Participation Group, the Carnegie Institution for Science, Carnegie Mellon University, Center for Astrophysics | Harvard & Smithsonian, the Chilean Participation, the French Participation Group, Instituto de Astrofísica de Canarias, The Johns Hopkins University, Kavli Institute for the Physics and Mathematics of the Universe (IPMU)/University of Tokyo, the Korean Participation Group, Lawrence Berkeley National Laboratory, Leibniz Institut für Astrophysik Potsdam (AIP), Max-Planck-Institut für Astronomie (MPIA Heidelberg), Max-Planck-Institut für Astrophysik (MPA Garching), Max-Planck-Institut für Extraterrestrische Physik (MPE), National Astronomical Observatories of China, New Mexico State University, New York University, University of Notre Dame, Observatário Nacional/MCTI, The Ohio State University, Pennsylvania State University, Shanghai Astronomical Observatory, United Kingdom Participation Group, Universidad Nacional Autónoma de México, University of Arizona, University of Colorado Boulder, University of Oxford, University of Portsmouth, University of Utah, University of Virginia, University of Washington, University of Wisconsin, Vanderbilt University, and Yale University.

DATA AVAILABILITY

The code developed for this work as well as the data sets used is available upon request.

REFERENCES

Alam S. et al., 2017, MNRAS, 470, 2617
Alam S. et al., 2021, Phys. Rev. D, 103, 083533
Alsing J., Heavens A., Jaffe A. H., 2017, MNRAS, 466, 3272
Asgari M. et al., 2021, A&A, 645, A104
Baker T., Ferreira P., Skordis C., 2014, Phys. Rev. D, 89, 024026
Benisty D., 2021, Phys. Dark Universe, 31, 100766
Betancourt M., 2017, preprint (arXiv:1701.02434)
Beutler F. et al., 2017, MNRAS, 466, 2242
Blake C. et al., 2012, MNRAS, 425, 405
Blanton M. R. et al., 2017, AJ, 154, 28
Bonilla A., Kumar S., Nunes R. C., 2021, Eur. Phys. J. C, 81, 127
Cai Y.-F., Khurshudyan M., Saridakis E. N., 2020, ApJ, 888, 62
Cimatti A., Daddi E., Renzini A., 2006, A&A, 453, L29
Colgáin E. Ó., Sheikh-Jabbari M. M., 2021, preprint (arXiv:2101.08565)
Colgate S. A., McKee C., 1969, ApJ, 157, 623
Dawson K. S. et al., 2016, AJ, 151, 44
DES Collaboration et al., 2021, Physical Review D, 105, 023520
Dialektopoulos K., Levi Said J., Mifsud J., Sultana J., Zarb Adami K., 2021, JCAP, 2022, 023
Drinkwater M. J. et al., 2010, MNRAS, 401, 1429
Efstathiou G., 2021, MNRAS, 505, 3866
Espejo J., Peirone S., Raveri M., Koyama K., Pogosian L., Silvestri A., 2019, Phys. Rev. D, 99, 023512
Font-Ribera A., McDonald P., Mostek N., Reid B. A., Seo H.-J., Slosar A., 2014, J. Cosmology Astropart. Phys., 2014, 023
Freedman W. L. et al., 2001, ApJ, 553, 47
Freedman W. L. et al., 2020, ApJ, 891, 57
García-García C., Ruiz Zapatero J., Alonso D., Bellini E., Ferreira P. G., Mueller E.-M., Nicola A., Ruiz-Lapuente P., 2021, JCAP, 2021, 030
Gelman A., Rubin D. B., 1992, Stat. Sci., 7, 457
Gelman A., Simpson D., Betancourt M., 2017, Entropy, 19, 555
Gerardi F., Martinelli M., Silvestri A., 2019, JCAP, 2019, 042
Gómez-Valent A., Amendola L., 2018, JCAP, 2018, 051
Gómez-Vargas I., Vázquez J. A., Medel Esquivel R., García-Salcedo R., 2021, preprint (arXiv:2104.00595)
Hamilton A. J. S., 1998, in Hamilton D., ed., Linear Redshift Distortions: a Review, Vol. 231, in 'The Evolving Universe'. Kluwer Academic, Dordrecht, p. 185
Hang Q., Alam S., Peacock J. A., Cai Y.-C., 2021, MNRAS, 501, 1481
Harris C. R. et al., 2020, Nature, 585, 357
Heymans C. et al., 2021, A&A, 646, A140
Hoffman M. D., Gelman A., 2011, preprint (arXiv:1111.4246)
Hou J. et al., 2021, MNRAS, 500, 1201
Hoyle F., Fowler W. A., 1960, ApJ, 132, 565
Hu W., Dodelson S., 2002, ARA&A, 40, 171
Jimenez R., Loeb A., 2002, ApJ, 573, 37
Joudaki S., Kaplinghat M., Keeley R., Kirkby D., 2018, Phys. Rev. D, 97, 123501
Kaiser N., 1987, MNRAS, 227, 1
Komatsu E. et al., 2009, ApJS, 180, 330
Krolewski A., Ferraro S., White M., 2021, JCAP, 2021, 028
L'Huillier B., Shafieloo A., Kim H., 2018, MNRAS, 476, 3263
Lesgourgues J., 2011, preprint (arXiv:1104.2932)
Lewis A., 2019, preprint (arXiv:1910.13970)
Liao K., Shafieloo A., Keeley R. E., Linder E. V., 2020, ApJ, 895, L29
Li E.-K., Du M., Zhou Z.-H., Zhang H., Xu L., 2021, MNRAS, 501, 4452
MacKay D. J. C., 2002, Information Theory, Inference & Learning Algorithms. Cambridge Univ. Press, USA
Margossian C. C., 2018, preprint (arXiv:1811.05031)
Moresco M., 2015, MNRAS, 450, L16
Moresco M., Jimenez R., Verde L., Pozzetti L., Cimatti A., Citro A., 2018, ApJ, 868, 84
Moresco M., Jimenez R., Verde L., Cimatti A., Pozzetti L., 2020, ApJ, 898, 82
Nesseris S., 2011, Journal of Physics Conference Series. 283, 012025
Nunes R. C., Vagnozzi S., 2021, MNRAS, 505, 5427
Park M., Raveri M., Jain B., 2021, Phys. Rev. D, 103, 103530
Peebles P. J. E., 1980, The Large-Scale Structure of the Universe. Princeton University Press, Princeton, NJ
Peebles P. J. E., Yu J. T., 1970, ApJ, 162, 815
Perenon L., Martinelli M., Ilić S., Maartens R., Lochner M., Clarkson C., 2021, preprint (arXiv:2105.01613)
Pesce D. W. et al., 2020, ApJ, 891, L1
Phillips M. M., Lira P., Suntzeff N. B., Schommer R. A., Hamuy M., Maza J., 1999, AJ, 118, 1766
Planck Collaboration VI et al., 2020, A&A, 641, A6
Pogosian L., Raveri M., Koyama K., Martinelli M., Silvestri A., Zhao G.-B., 2021, preprint (arXiv:2107.12992)
Rajpaul V., 2012, preprint (arXiv:1202.1643)
Rasmussen C. E., Williams C. K. I., 2006, Gaussian Processes for Machine Learning., Adaptive Computation and Machine Learning. MIT Press, Cambridge, USA
Raveri M., Bull P., Silvestri A., Pogosian L., 2017, Phys. Rev. D, 96, 083509
Raveri M. et al., 2021, preprint (arXiv:2107.12990)
Riess A. G., 2000, in Courteau S., Willick J., eds, ASP Conf. Ser.Vol. 201, Cosmic Flows Workshop. Astron. Soc. Pac., San Francisco, p. 80
Riess A. G., Casertano S., Yuan W., Bowers J. B., Macri L., Zinn J. C., Scolnic D., 2021, ApJ, 908, L6
Ruiz-Zapatero J. et al., 2021, A&A, 655, A11
Salvatier J., Wiecki T., Fonnesbeck C., 2015, preprint (arXiv:1507.08050)
Scolnic D. M. et al., 2018, ApJ, 859, 101
Seikel M., Clarkson C., Smith M., 2012, JCAP, 2012, 036
Shafieloo A., Kim A. G., Linder E. V., 2012, Phys. Rev. D, 85, 123530
Shafieloo A., L'Huillier B., Starobinsky A. A., 2018, Phys. Rev. D, 98, 083526
Shah P., Lemos P., Lahav O., 2021, A&AR, 29, 9
Stahl B. E., de Jaeger T., Boruah S. S., Zheng W., Filippenko A. V., Hudson M. J., 2021, MNRAS, 505, 2349
The Theano Development Team et al., 2016, preprint (arXiv:1605.02688)
Thomas J. et al., 2011, MNRAS, 415, 545
Tully R. B., Courtois H. M., Sorce J. G., 2016, AJ, 152, 50
Vagnozzi S., Loeb A., Moresco M., 2021, ApJ, 908, 84

Virtanen P. et al., 2020, Nature Methods, 17, 261
White M. et al., 2021, JCAP, 2022, 007
Yang Y., Gong Y., 2021, MNRAS, 504, 3092
Zhang M.-J., Li H., 2018, Eur. Phys. J. C, 78, 460

APPENDIX A: FULL RESULTS

In this appendix, we present the full set of posterior distributions for all cosmological parameters and for each of the combinations of data sets and analysis choices studied here. In Fig. A1, we show the marginalized posteriors resulting of the different combinations of data sets. In Fig. A2, we show the marginalized posteriors resulting of the different analysis choices for the entire combination of data sets juxtaposed. In Fig. A3, we show the marginalized posteriors using the synthetic DESI data set.

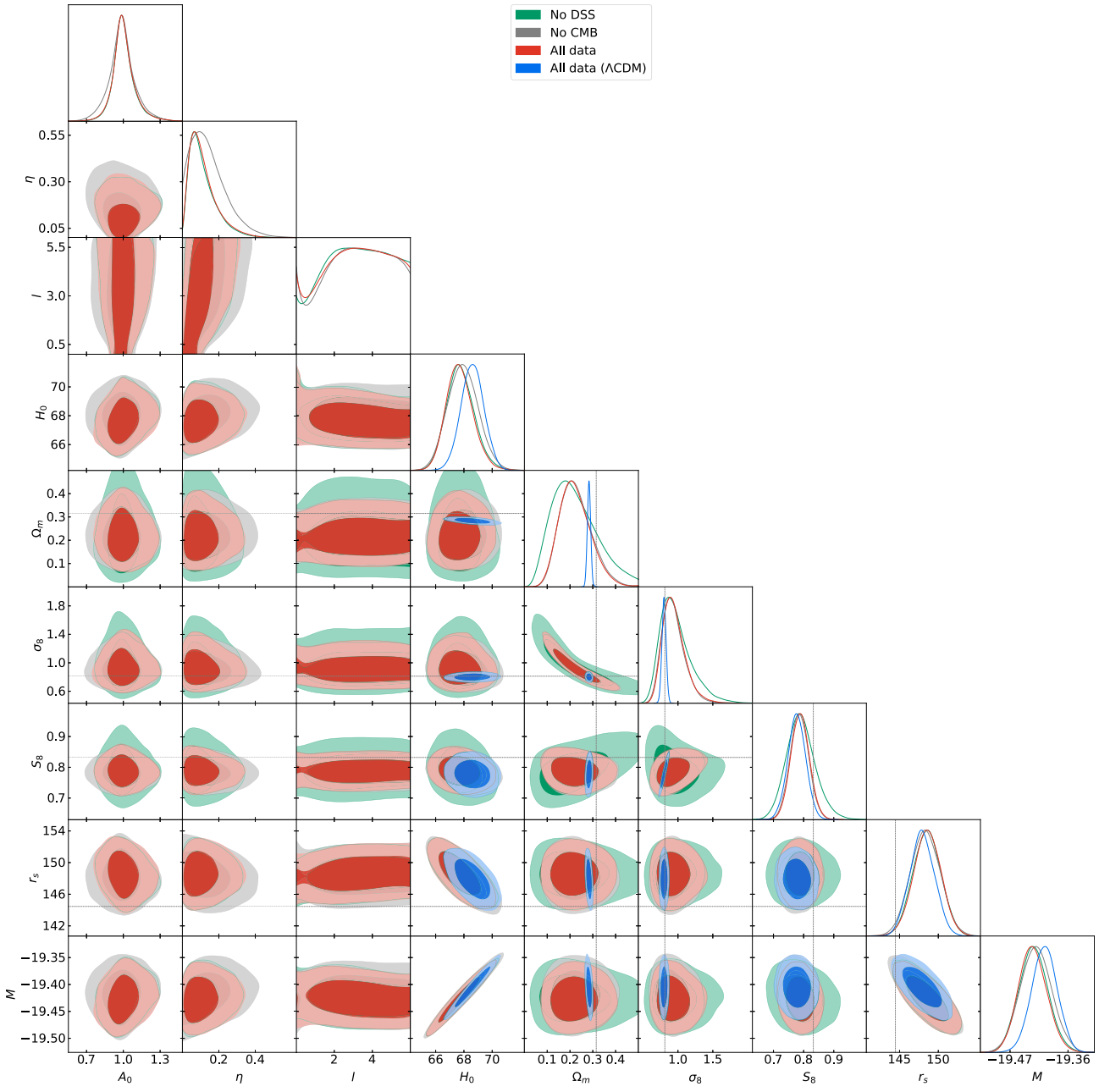

Figure A1. Comparison of the full posterior distributions of the analysis of all the considered data (red), the analysis of all data except for the DSS data set (green), the analysis of all data except for the CMB data set (grey), and the ΛCDM analysis of the data (blue). The parameters displayed are the GP hyperparameters η and l; the cosmological parameters $H(z = 0)$, $\Omega_{\rm m}$, $\sigma_{8,}$ and S_8 in this order; and the nuisance parameters $r_{\rm s}$ and M. Central panels show the 2D histograms of the different parameter combinations while diagonal panels show one-dimensional (1D) histograms.

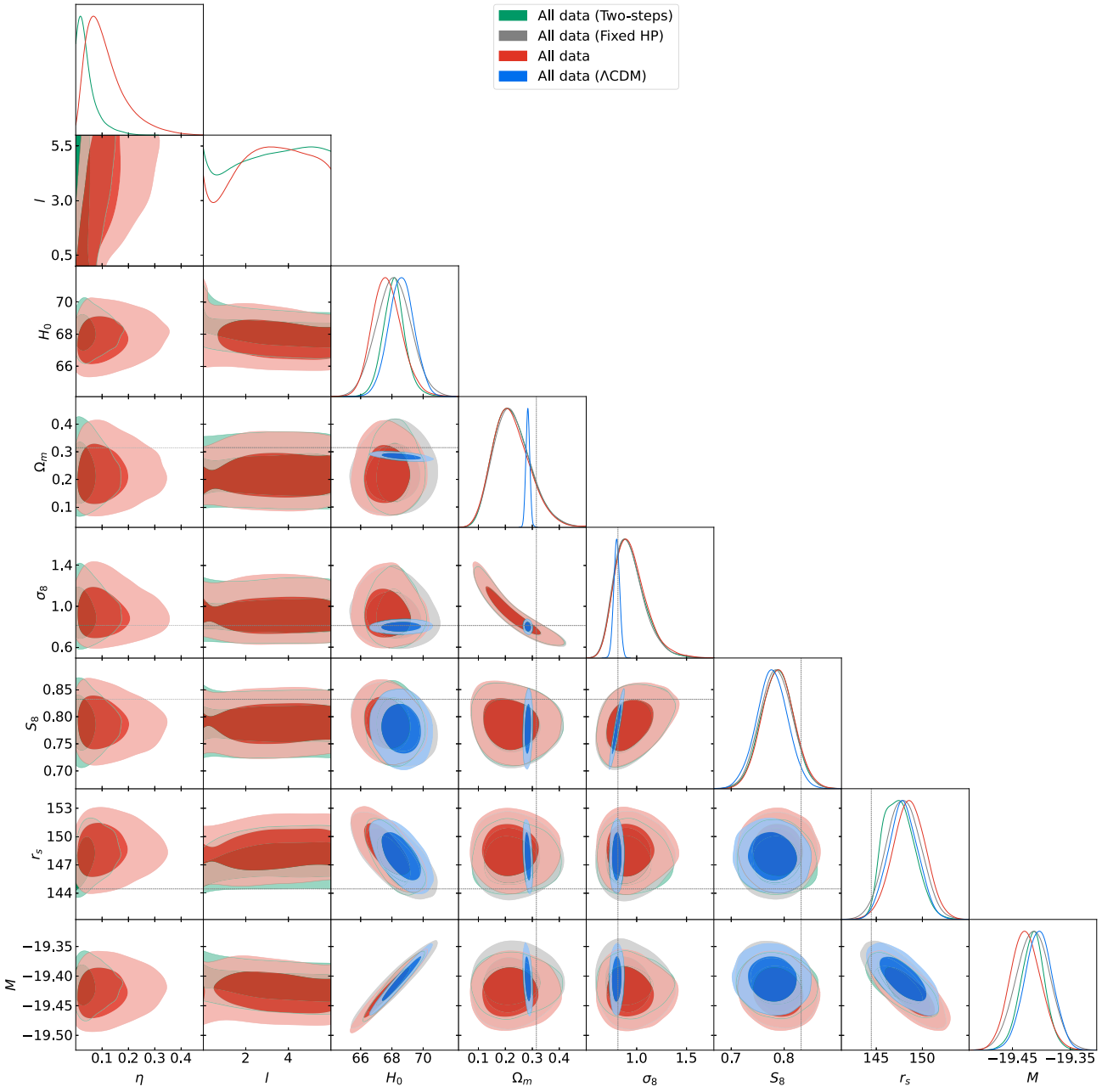

Figure A2. Comparison of the full posterior distributions of the standard analysis of all considered data (red), the Two-Steps analysis constraints (green), the fixed hyperparamters analysis (grey), and the ΛCDM analysis of the data (blue). The parameters displayed are the GP hyperparameters η and l; the cosmological parameters $H(z = 0)$, $\Omega_{\rm m}$, σ_8, and S_8 in this order; and the nuisance parameters $r_{\rm s}$ and M. Central panels show the 2D histograms of the different parameter combinations while diagonal panels show 1D histograms.

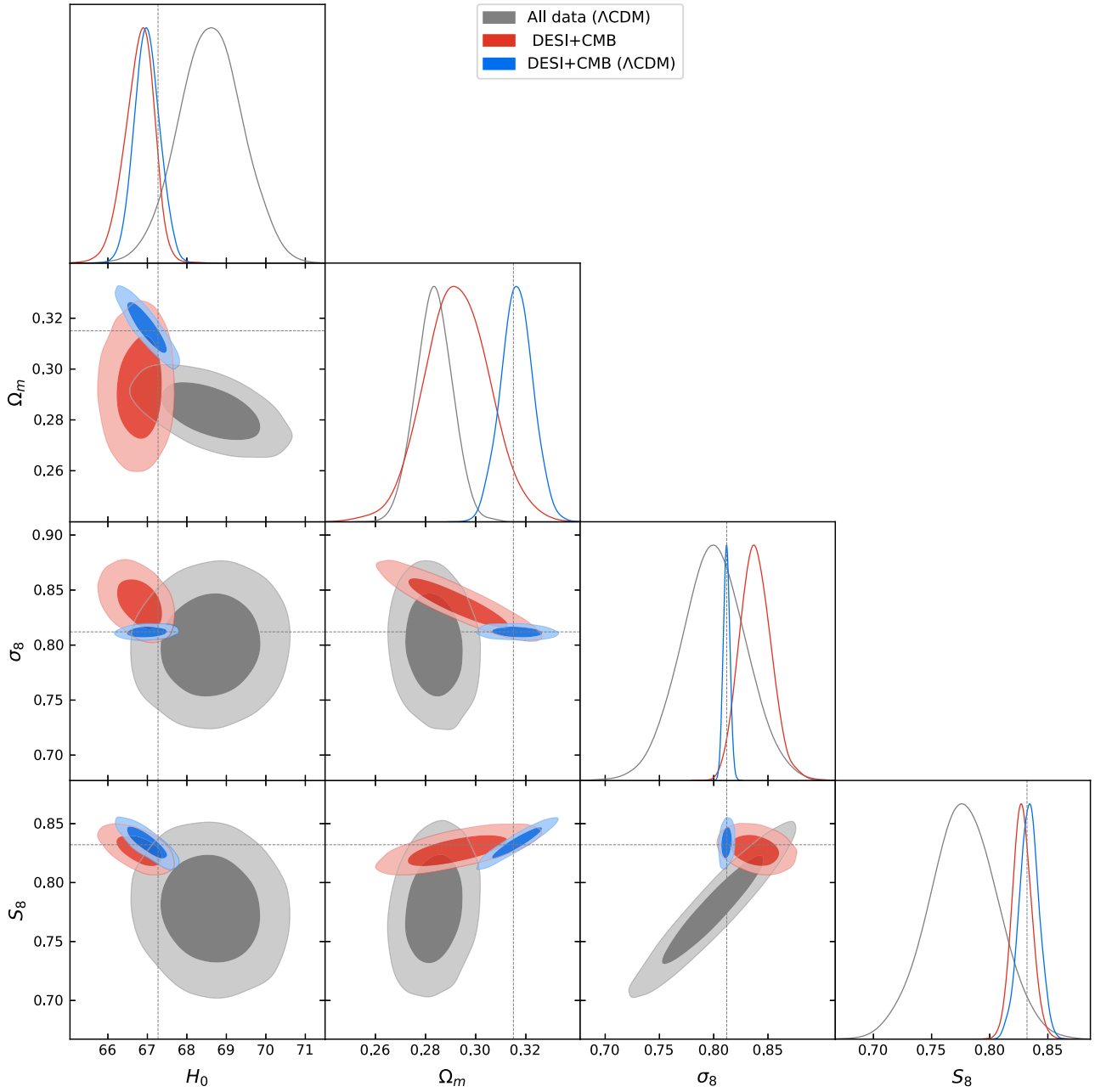

Figure A3. Comparison of the full posterior distributions between the DESI + CMB analysis (blue) and the ΛCDM analysis of present data (red). The parameters displayed are the cosmological parameters $H(z = 0)$, Ω_m, Ω_b, σ_8, and S_8 in this order. Central panels show the 2D histograms of the different parameter combinations while diagonal panels show 1D histograms.

APPENDIX B: ALTERNATIVE ANALYSES

In this appendix, we present the impact on the constraints on $\delta H(z)$ of the different analysis choices enumerated at the end of Section 2. Specifically, we studied the effect of fixing the value of the hyperparameters η and l to the values listed in Table 2 (labeled 'Fixed HP') and the effect of performing a two-step analysis (labeled 'Two-Steps'). In Fig. B1, we can observe how fixing the hyperparameters drastically changes the shape of $\delta H(z)$. On the one hand, fixing the value of η prevents the low redshift data from constraining its value. Meaning that in the absence of data (i.e. for $z > 2.5$), the GP amplitude is constant and completely dominated by the prior as opposed to being inferred from the low redshift data. On the other hand, fixing $l = 1.0$ imposes a particular scale of correlation on the expansion history.

Performing a two-step analysis produces qualitatively similar results to simultaneously re-scaling the GP mean with the parameter A_0. However, the two-step analysis produces significantly tighter constraints on $\delta H(z)$ due to the breaking of the degeneracies between A_0 and $\delta H(s)$. This can be observed in the two-step analysis recovering a three times smaller value of the hyperparameter η and a four times smaller value of the $\overline{\sigma}(\delta H(s))$ statistic with respect to simultaneously re-scaling the mean. This is due to the fact that the parameter A_0, used to re-scale the mean, is partially degenerate with

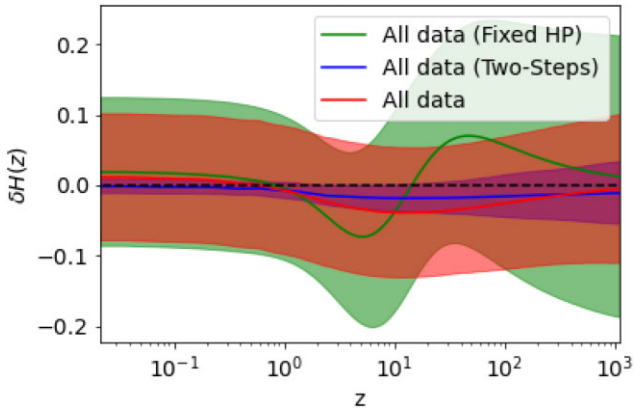

Figure B1. Comparison of the constraints for the cosmological functions $\delta H(z)$ between the standard analysis (red), the fixed hyperparameters analysis (green, Fixed HP), and the Two-Steps analysis (blue) of all the considered data.

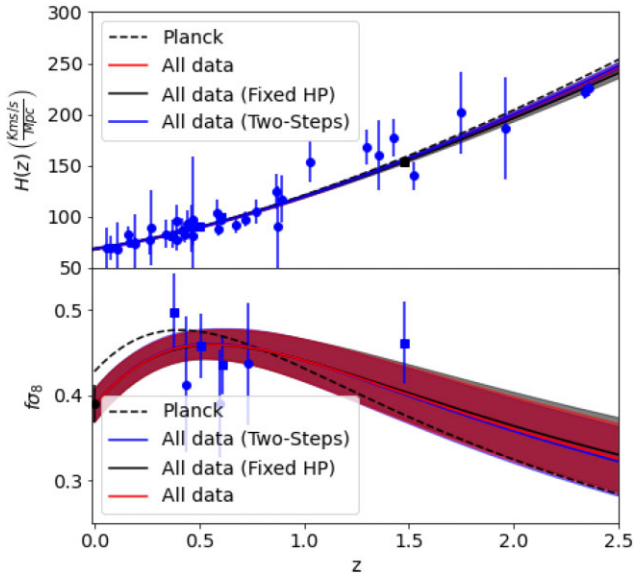

Figure B2. Comparison of the constraints for the cosmological functions $H(z)$ and $f\sigma_8$ (top and bottom panels, respectively) between the standard analysis (red), the Two-Steps analysis (blue), and the fixed hyperparameters analysis (grey) of all considered data. Solid lines represent the mean of the GPs at each redshift. Contours represent the associated 1σ confidence regions. The dashed black lines show the *Planck* 2018 prediction for each cosmological function.

the amplitude of $\delta H(z)$ and thus with η, introducing a greater degree of uncertainty.

If instead of looking at $\delta H(z)$ we focus on the cosmological functions $H(z)$ and $f\sigma_8$, we find that the predictions of the fiducial and alternative analyses for the cosmological functions are statistically compatible up to 1σ for all redshifts. This can be observed in Fig. B2. This means that despite the fact that the analysis choices can have a severe impact in the shape of $\delta H(z)$, once $\delta H(z)$ is converted into the cosmological functions (i.e. the quantities actually being matched to the data), the standard and alternative analyses converge to similar predictions.

Reassuringly, the constraints for the cosmological parameters Ω_m, σ_8, and S_8 are virtually unaffected by either fixing the hyperparameters or choosing a Two-Steps analysis over simultaneously fitting the mean of the GP. This can be seen both in Fig. 5. It would be interesting to understand up to what degree of uncertainty on $H(z)$ one recovers the same constraints for these parameters. We leave this for future work.

Preliminary analyses showed that if instead of constraining the cosmological parameters of the mean of the GP in a separate step they were sampled simultaneously with the GP in a single step, one obtains a similar level of uncertainty to that introduced by the A_0 parameter. None the less, A_0 has the added benefit of not duplicating parameters. For this reason, we favour the scaling with A_0 as our main methodology.

APPENDIX C: VALIDITY OF COSMOLOGICAL INFERENCE

In order to verify that the cosmological constraints obtained by this methodology are not biased by the choice of mean for the GP, we performed a blind analysis of mock data generated from five known cosmologies different from *Planck* 2018 named Cosmo1-5. The mock data were generated following the errors and redshift of current measurements to ensure the validity of the methodology when applied to real data. We display the chosen cosmological parameter values in Table C1. Cosmo1 corresponds to a *Planck* 2018 cosmology. Cosmo2 poses a slightly higher value of Ω_m with respect to the previous. Cosmo3 has an equation of state parameter $w_0 > -1$. Cosmo4 has significantly larger value of H_0 than *Planck* 2018. Finally, Cosmo5 has a significantly larger value of Ω_m than *Planck* 2018.

Figs C1–C5 show the 1D posterior distributions obtained from analysing one random realization of mock data from each of the cosmologies considered. Our results show that for all five scenarios our methodology returns cosmological constraints statistically compatible with the set of cosmological parameters used to generate the respective data sets. This can be observed in the fact that for all cases the 2 σ contours of each cosmological parameter contain value of the underlying cosmology.

However, previous iterations of our methodology where the value of the parameter A_0 was kept fixed at $A_0 = 1$ showed significant biases in their cosmological parameter inference with respect the input cosmological parameters. This biases manifested specially strongly in the constraints for the parameter H_0. This stresses the need of choosing a mean that does not systematically underpredict or overpredict the data being fitted with GP, specially if there are sections in the GP domain in which data are not present. In this range, the GP returns to its prior distribution, and thus a biased mean results on biased cosmological parameters and functions.

Table C1. Values of the cosmological parameters used to define the alternative cosmologies used to generate the mock data for the blindfold analysis.

Parameter	Cosmo1	Cosmo2	Cosmo3	Cosmo4	Cosmo5
Ω_m	0.316	0.356	0.316	0.316	0.474
Ω_b	0.050	0.056	0.050	0.050	0.070
Ω_Λ	0.683	0.644	0.683	0.683	0.526
H_0	67.27	67.27	67.27	74	67.27
σ_8	0.811	0.811	0.811	0.811	0.811
w_0	−1	−1	−0.9	−1	−1

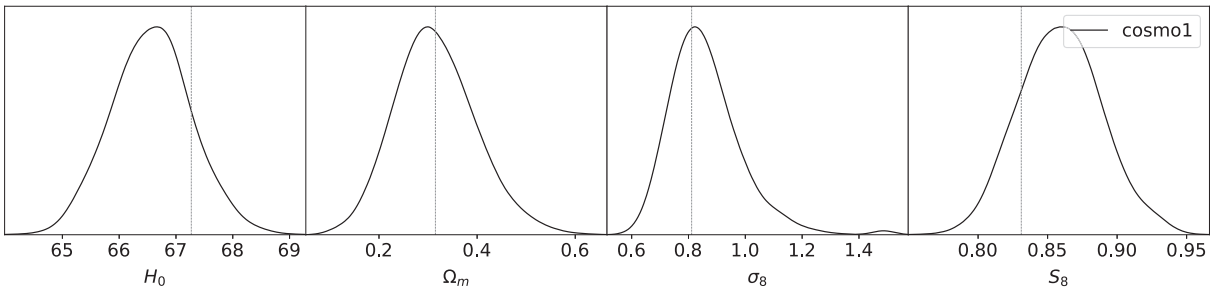

Figure C1. 1D Posterior distributions for the cosmological parameters $H(z = 0)$, $\Omega_{\rm m}$, σ_8, and S_8 resulting from the blind analysis of one random realization of mock data generated from Cosmo1. Dotted lines shows the value of the cosmological parameters used to generate the random realization of the data. Central panels show the 2D histograms of the different parameter combinations while diagonal panels show 1D histograms. Darker contours cover the 1σ CL region, whereas lighter ones cover the 2σ region.

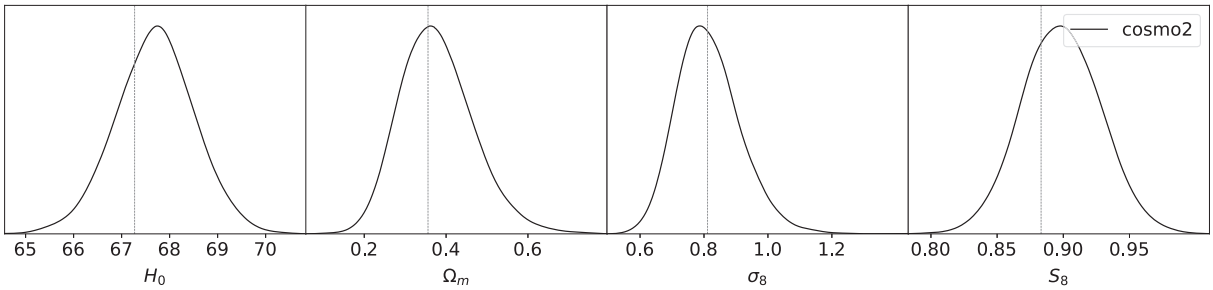

Figure C2. 1D Posterior distributions for the cosmological parameters $H(z = 0)$, $\Omega_{\rm m}$, σ_8, and S_8 resulting from the blind analysis of one random realization of mock data generated from Cosmo2. Dotted lines shows the value of the cosmological parameters used to generate the random realization of the data. Central panels show the 2D histograms of the different parameter combinations while diagonal panels show 1D histograms. Darker contours cover the 1σ CL region, whereas lighter ones cover the 2σ region.

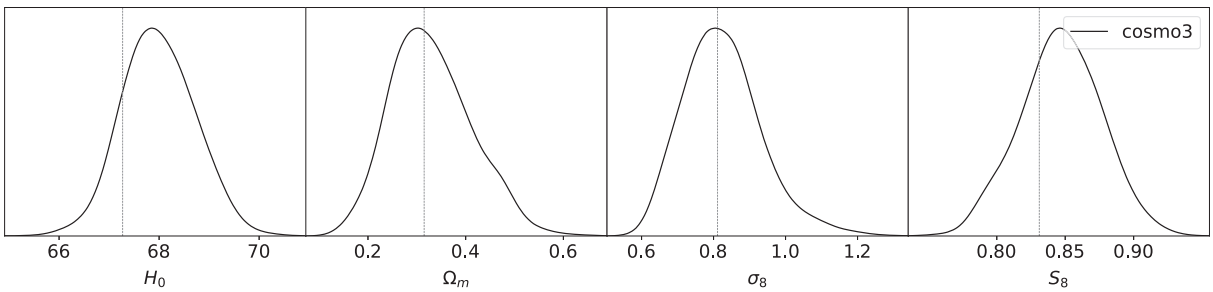

Figure C3. 1D Posterior distributions for the cosmological parameters $H(z = 0)$, $\Omega_{\rm m}$, σ_8, and S_8 resulting from the blind analysis of one random realization of mock data generated from Cosmo3. Dotted lines shows the value of the cosmological parameters used to generate the random realization of the data. Central panels show the 2D histograms of the different parameter combinations while diagonal panels show 1D histograms. Darker contours cover the 1σ CL region, whereas lighter ones cover the 2σ region.

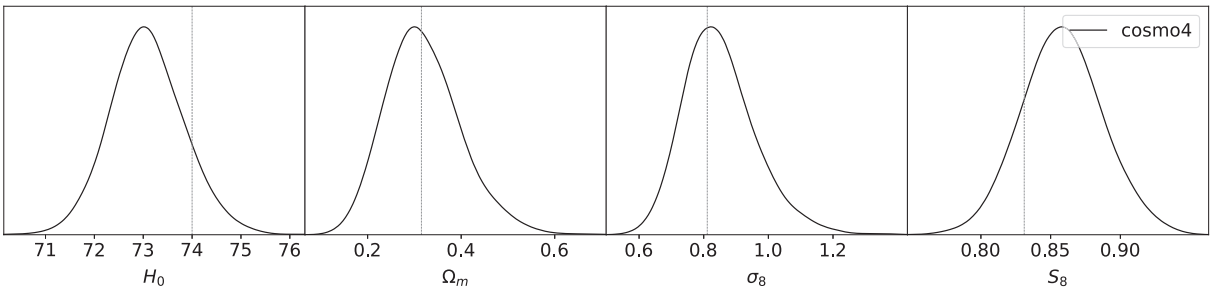

Figure C4. 1D Posterior distributions for the cosmological parameters $H(z = 0)$, $\Omega_{\rm m}$, σ_8, and S_8 resulting from the blind analysis of one random realization of mock data generated from Cosmo4. Dotted lines shows the value of the cosmological parameters used to generate the random realization of the data. Central panels show the 2D histograms of the different parameter combinations while diagonal panels show 1D histograms. Darker contours cover the 1σ CL region, whereas lighter ones cover the 2σ region.

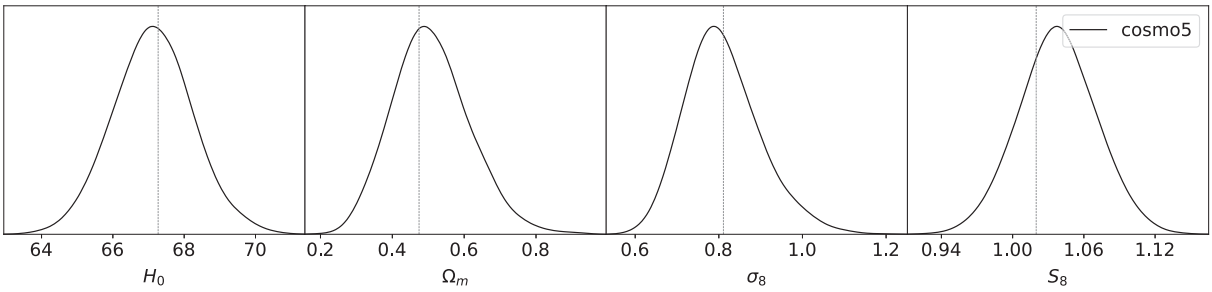

Figure C5. 1D Posterior distributions for the cosmological parameters $H(z = 0)$, $\Omega_{\rm m}$, σ_8, and S_8 resulting from the blind analysis of one random realization of mock data generated from Cosmo5. Dotted lines shows the value of the cosmological parameters used to generate the random realization of the data. Central panels show the 2D histograms of the different parameter combinations while diagonal panels show 1D histograms. Darker contours cover the 1σ CL region, whereas lighter ones cover the 2σ region.

APPENDIX D: USING HMC

In this work, we employed the No U-Turn sampler (NUTS), a self-tuning variant of the Hamiltonian Monte Carlo (HMC) sampler, implemented in PyMC3. In this implementation, chains are divided in two stages: a tuning phase and an exploration phase. During the tuning phase, the NUTS algorithm tunes the so-called 'mass matrix'. The mass matrix is the covariance matrix of the conjugate momentum parameters and plays a role in how effectively the different energy values of the Hamiltonian are explored. Therefore, allowing for a sufficiently long tuning phase results in a well-calibrated mass matrix, which then translates into an efficient exploration stage of the chain.

However, even when equipped with a well-informed mass matrix, HMC can be turned unreliable and inefficient if one overlooks the effectiveness of the numerical methods being used to resolve the Hamiltonian trajectories. Thus, a poor configuration of said methods can lead to the numerical solvers being unable to resolve the trajectories. These instances are known as divergences. Divergences have the undesired effects of (a) making the sampling process inefficient and (b) biasing the resulting posteriors. On the one hand, divergences make the sampling process inefficient as their fraction of the total number of steps needs to be rejected. On the other hand, divergences break the geometry ergodicity of sampler (i.e. its ability to explore the whole parameter space) such that stationary distribution of the Markov chains is no longer guaranteed to be target distribution. Divergences tend to occur in those areas of the likelihood function with high curvature (i.e. the slopes of the distributions). Thus, divergences can lead to artificial constraining power by virtue of the majority of the samples clustering at the regions of low-likelihood curvature (i.e. the top of posterior distribution and the tails), creating a fake abrupt drop of the probability density outside the vicinity of the area of maximum likelihood. The NUTS implementation of PyMC3 allows to control such aspects by what it is referred to as the 'target acceptance probability' (the desired probability of the next step of the Monte Carlo chain being accepted). PyMC3 tunes the step size of the numerical methods during the tuning phase of the algorithm such that the desired target acceptance probability is obtained. A target acceptance probability of 1 is thus equivalent to an infinitesimally small step size that perfectly resolves the Hamiltonian trajectories and for which no divergences occur. However, it is easy to see that such a small step size would result in an extremely slow exploration of the posterior. Therefore, it is vital to strike a balance between reliability and speed. In this work, we find that for our likelihood, a target acceptance probability of 97 per cent results in both efficient and reliable exploration of the posterior distribution.

In Fig. D1, we illustrate the severity of the bias that such divergences can introduce in the apparent constraining power of the data on the GP described in our methodology. In this figure, we can see how results obtained with a target acceptance probability of 90 per cent are around 1.5 times wider than those obtained with a target acceptance probability of 97 per cent for which the number of divergences was reduced 20-fold to around 0.5 per cent divergent steps in our chains.

Finally, it is also important to mention that raising the target acceptance probability reduced the computational time required by the chains ran for this paper by an order of magnitude, proving once again the importance of tuning the numerical methods employed by the sampler.

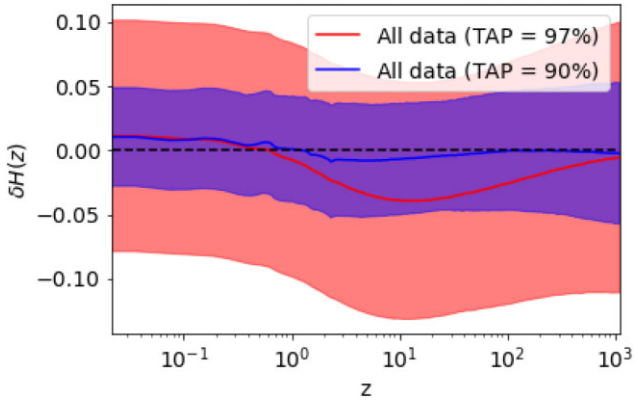

Figure D1. Comparison between the $\delta H(z)$ constraints obtained from two different HMC runs, one in which the target acceptance probability was set to 90 per cent and one in which it was set to 97 per cent. In both cases, all present data were considered. Solid lines represent the mean of the GPs at each redshift. Contours represent the associated 1σ confidence regions.

This paper has been typeset from a TEX/LATEX file prepared by the author.